Gas emissions and sub-surface architecture of fault-controlled geothermal systems: a case study of the North Abaya geothermal area

William Hutchison[1], Euan Ogilvie[1], Yafet G Birhane[2], Peter H Barry[3], Tobias P. Fischer[4], Chris J Ballentine[5], Darren J Hillegonds[5], Juliet Biggs[6], Fabien Albino[7], Chelsea Cervantes[8], Snorri Gubrandsson[8], Fátima Viveiros[9], Egbert Jolie[10], and Giacomo Corti[11]

[1]University of St Andrews
[2]CRPG, Université de Lorraine
[3]Woods Hole Oceanographic Institution
[4]University of New Mexico
[5]University of Oxford
[6]University of Bristol, UK
[7]University of Grenoble Alpes, ISTerre
[8]Reykjavik Geothermal
[9]Instituto de Investigação em Vulcanologia e Avaliação de Riscos
[10]GFZ German Research Centre For Geosciences
[11]Consiglio Nazionale delle Ricerche

December 9, 2022

Abstract

East Africa hosts significant reserves of untapped geothermal energy. Most exploration has focused on geologically young (<1 Ma) silicic caldera volcanoes, yet there are many sites of geothermal potential where there is no clear link to an active volcano. The origin and architecture of these systems is poorly understood. Here, we combine remote sensing and field observations to investigate a fault-controlled geothermal play located north of lake Abaya in the Main Ethiopian Rift. Soil gas CO2 and temperature surveys were used to examine permeable pathways and showed elevated values along a ˜110 m high fault which marks the western edge of the Abaya graben. Ground temperatures are particularly elevated where multiple intersecting faults form a wedged horst structure. This illustrates that both deep penetrating graben bounding faults and near-surface fault intersections control the ascent of hydrothermal fluids and gases. Total CO2 emissions along the graben fault are ˜300 t d–1; a value comparable to the total CO2 emission from silicic caldera volcanoes. Fumarole gases show δ13C of –6.4 to –3.8 values of 3.84–4.11 RA, indicating a magmatic source originating from an admixture of upper mantle and crustal helium. Although our model of the North Abaya geothermal system requires a deep intrusive heat source, we find no ground deformation evidence for volcanic unrest nor recent volcanism. This represents a key advantage over the active silicic calderas that typically host these resources and suggests that fault-controlled geothermal systems offer viable prospects for further exploration and development.

Hosted file

`951555_0_art_file_10518255_rmkg73.docx` available at https://authorea.com/users/565031/articles/612027-gas-emissions-and-sub-surface-architecture-of-fault-controlled-geothermal-systems-a-case-study-of-the-north-abaya-geothermal-area

Gas emissions and sub-surface architecture of fault-controlled geothermal systems: a case study of the North Abaya geothermal area

William Hutchison[1], Euan R. D. Ogilvie[1], Yafet G. Birhane[2], Peter H. Barry[3], Tobias P. Fischer[4], Chris J. Ballentine[5], Darren J. Hillegonds[5], Juliet Biggs[6], Fabien Albino[6,7], Chelsea Cervantes[8] and Snorri Guðbrandsson[8]

[1]School of Earth and Environmental Sciences, University of St Andrews, St Andrews, UK.
[2]School of Earth Sciences, University of Addis Ababa, Addis Ababa, Ethiopia
[3]Woods Hole Oceanographic Institution, Woods Hole, Massachusetts, USA.
[4]Department of Earth and Planetary Sciences, University of New Mexico, Albuquerque, NM, USA
[5]Department of Earth Sciences, University of Oxford, South Parks Road, Oxford OX1 3AN, UK.
[6]COMET, School of Earth Sciences, University of Bristol, Bristol, UK.
[7]Institut des Sciences de la Terre, Universite Grenoble Alpes, Grenoble, France.
[8]Reykjavik Geothermal Ltd., Reykjavik, Iceland.

Key Points:

- First conceptual model of a fault-controlled magmatic geothermal resource in the East African Rift
- Focus on North Abaya in the Main Ethiopian Rift and show that deep hydrothermal upflow is concentrated along a major graben bounding fault
- Magmatic CO_2 emissions along this fault are ~300 t d^{-1} and comparable to average values from the world's sub-aerial volcanoes

Abstract

East Africa hosts significant reserves of untapped geothermal energy. Most exploration has focused on geologically young (<1 Ma) silicic caldera volcanoes, yet there are many sites of geothermal potential where there is no clear link to an active volcano. The origin and architecture of these systems is poorly understood. Here, we combine remote sensing and field observations to investigate a fault-controlled geothermal play located north of lake

Abaya in the Main Ethiopian Rift. Soil gas CO_2 and temperature surveys were used to examine permeable pathways and showed elevated values along a ~110 m high fault which marks the western edge of the Abaya graben. Ground temperatures are particularly elevated where multiple intersecting faults form a wedged horst structure. This illustrates that both deep penetrating graben bounding faults and near-surface fault intersections control the ascent of hydrothermal fluids and gases. Total CO_2 emissions along the graben fault are ~300 t d^{-1}; a value comparable to the total CO_2 emission from silicic caldera volcanoes. Fumarole gases show $\delta^{13}C$ of –6.4 to –3.8 ‰ and air-corrected $^3He/^4He$ values of 3.84–4.11 R_A, indicating a magmatic source originating from an admixture of upper mantle and crustal helium. Although our model of the North Abaya geothermal system requires a deep intrusive heat source, we find no ground deformation evidence for volcanic unrest nor recent volcanism. This represents a key advantage over the active silicic calderas that typically host these resources and suggests that fault-controlled geothermal systems offer viable prospects for further exploration and development.

1. Introduction

The East African Rift System (EARS) hosts a wide range of volcanoes and geothermal resources (Biggs et al., 2021). Although these systems offer huge benefits in terms of clean, renewable energy few sites have been fully explored, let alone developed (Kombe and Muguthu, 2018). Over the last few decades new insights into the origin, architecture and stability of East Africa's geothermal resources have come from studies of ground deformation (e.g., Biggs et al., 2009, 2011; Temtime et al., 2018; Albino and Biggs, 2021), magnetotellurics (e.g. Samrock et al., 2015, 2018); seismicity (e.g., Simiyu and Keller, 2000; Wilks et al., 2017; Nowacki et al., 2018), gas emissions (e.g., Hutchison et al., 2015, 2016) and fluid geochemistry (e.g., Pürschel et al., 2013). These studies emphasise that the most promising geothermal resources are associated with volcanic calderas. In these systems, hydrothermal fluids are derived from meteoric sources (Darling et al., 1996; Rango et al., 2010) while the heat is supplied by long-lived silicic magma reservoirs (Iddon et al., 2019). High temperature, convecting geothermal fluids are trapped beneath a relatively shallow (0.5–2 km deep) impermeable clay cap layer and tectonic faults play a key role in directing the flow of these fluids towards the surface (Hutchison et al., 2015; Samrock et al., 2018). Although the deep (km-scale) architecture of these volcanic-geothermal systems is best imaged by magnetotellurics, high-spatial resolution (~10–50 m) gas surveys are particularly powerful at identifying permeability and pinpointing drilling locations (Jolie et al., 2019).

Though many of East Africa's geothermal resources fit this model and are intimately associated with silicic caldera complexes there are various sites which show geothermal manifestations and high fluxes of magmatic volatiles, but no surface volcanism. These areas are associated with tectonic faulting and include the Natron and Magadi basins at Kenya-Tanzania border (Lee et al., 2016, 2017; Muirhead et al., 2016) and the Habilo area NW of Fantale in the Main Ethiopian Rift (Hunt et al., 2017). To date, few studies have investigated the architecture and potential of these fault-controlled geothermal systems. However, when compared to the silicic calderas (which pose considerable volcanic eruption hazards that could lead to damage and disruption of geothermal infrastructure, Fontijn et al., 2018; Clarke et al., 2020; Tierz et al., 2020), these fault-controlled geothermal areas are potentially much lower risk and therefore safer options for exploration, investment and development.

Here, we bring together new remote sensing and gas emission data from the North Abaya geothermal area in the Main Ethiopian Rift (MER) which is a fault-controlled geothermal play that shows no surface volcanic edifice. North Abaya is consistently highlighted as one of Ethiopia's key geothermal prospects (Burnside et al., 2021), and although previous studies have investigated regional volcano-tectonic activity (Corti et al., 2013, Ogden et al., 2021) and documented surface geothermal manifestations (i.e., hot springs and fumaroles, Craig et al., 1977; Chernet, 2011; Minissale et al., 2017) there is no conceptual model to understand the heat source, fluid flow, gas emissions and geothermal potential of the resource. We show that despite a clear lack of surface volcanism, a deep magmatic source is required, and that large offset graben bounding faults play a key role in channelling gas and hydrothermal fluids toward the surface. Gas emissions are comparable to sites of proven geothermal resources in Ethiopia (e.g., the silicic caldera of Aluto) and while there are fundamental differences between the North Abaya geothermal play and the silicic calderas, our conceptual model suggests there is great potential for further exploration and development.

2. Geological setting

2.1 The Main Ethiopian Rift (MER)

The MER (Fig. 1) is the northernmost segment of the EARS and accommodates E-W extension between the Nubia and Somalia Plates (Corti, 2009). The region is extending at 4–6 mm yr^{-1} (e.g., Saria et al., 2014) and this is accommodated by both faulting and magmatic intrusion (Ebinger, 2005; Keir et al., 2006; Corti et al., 2013). The MER is subdivided into northern (NMER), central (CMER), and southern (SMER) segments and there is a broad consensus that rift maturity decreases southwards (Agositini et al., 2011). One of most the fundamental differences is the style and location of volcano-tectonic activity. In the NMER, border faults, with large vertical offsets >100 m, define the boundaries of the rift but are largely abandoned (Wolfenden et al., 2004; Casey et al., 2006; Keir et al., 2006). Active seismicity and magmatic intrusion in the NMER is instead focused along the axis of the rift (Ebinger & Casey, 2001; Kendall et al., 2005; Keir, et al., 2006) in a region commonly referred to as the Wonji Fault Belt (e.g., Mohr, 1967; Gibson, 1969; Boccaletti et al., 1999). In the SMER, the focus of this study, geological and geophysical data show very different patterns and indicate that border faults still accommodate significant extension (Pizzi et al., 2006; Agostini et al., 2011; Kogan et al., 2012; Molin and Corti, 2015). Recent volcanism is co-located with border faults along the rift margins (Rooney et al., 2011; Corti et al., 2013), again, contrasting with the focused axial magmatism observed in more northerly segments of the MER.

Bimodal volcanism due to rift-related magmatic intrusion is abundant throughout the MER. Mafic lava flows and scoria cone fields are abundant, as are highly evolved peralkaline rhyolitic complexes (Gibson, 1969; Hutchison et al., 2015: Hunt et al., 2019, 2020). Primitive mantle-derived melts are stored at depths of at ~15 km beneath the surface where they form dyke complexes and undergo mafic fractionation (Iddon and Edmonds, 2020). Such dykes are thought to then undergo either rapid transition to the surface where they erupt as monogentic cinder cones (Rooney et al., 2011; Mazzarini et al., 2013) or are focused towards shallow (~5 km deep) silicic magma bodies where they undergo more extensive crystal fractionation to form trachytic and rhyolitic melts (Peccerillo et al., 2003; Rooney et al., 2012; Iddon et al., 2019). These erupt to form a thick pile of coalescing rhyolitic lava flows and domes, pumice cones, and pyroclastic deposits (Hutchison et al., 2015, 2016; Hunt et al., 2019).

2.2 Volcanic and tectonic features of the North Abaya geothermal area

The North Abaya geothermal area is located in the Soddo area of the SMER (Corti et al., 2013, Figs 1, 2a). Here, like many areas of the MER, surface geology is typified by NE-SW trending faults and bimodal volcanism (primarily mafic scoria cone fields and larger, 3–15 km wide, silicic centres and calderas). Mapping of regional fault structures by Chernet (2011) and Corti et al. (2013) identified a prominent network of right-stepping *en echelon* normal or oblique faults, with vertical offsets generally <100 m, and lengths of 1–10 km. Unlike other sections of the rift, where there is often a single well-defined border fault with a large vertical offset (>>100 m), the North Abaya area reveals a dense concertation of border faults which result in a staggered uplift towards the rift flank over 10–20 km (Corti et al., 2013, Fig. 2b). Across this zone of border faults three prominent graben structures are observed and from west to east these are the Salewa Dore-Hako graben, the Abaya graben and Chewkare graben (Fig. 2c, Section 4.1). Tectonic activity in this region has occurred through the Late Pleistocene-Holocene (Corti et al., 2013) and there is ongoing seismicity associated with this border fault swarm (Ogden et al., 2021).

Recent volcanism is concentrated in the Salewa Dore-Hako Graben and includes isolated mafic scoria cones and the 3.5 km wide, 250 m high Salewa Dore-Hako rhyolite complex (Fig. 2a).

Both the mafic and silicic vents show alignment with nearby graben faults indicating important fault controls on magma ascent (noted previously by Corti et al., 2013, and at other Ethiopian rift volcanoes, c.f. Hutchison et al., 2015; Hunt et al., 2020). Although robust age constraints on volcanism in North Abaya are currently lacking, the co-location of fumaroles at mafic and silicic vents attests to very recent, most likely Holocene, eruptive activity probably coincident with episodes of faulting (Corti et al., 2013).

Various geothermal features have been identified in the North Abaya area (summarized in Fig. 2a). Of these the most vigorous thermal manifestations (hot springs and fumaroles with temperatures up to ~95 ºC, Chernet, 2011) are found 1–2 km north of Lake Abaya along a major fault the that bounds the Abaya graben (herein referred to as West Abaya graben fault, Fig. 2b). Steam vents have also been observed at the summit of the Salewa Dore-Hako rhyolitic complex but are of more limited areal extent and intensity with temperatures of 40–90 ºC. Geochemical analyses of spring waters in the Abaya region show meteoric isotope compositions with a dominant Na and HCO_3 composition (indicative of water-rock interaction at depth, Minissale et al., 2017). Fumarole gases are notable for their high CO_2 contents (80–95 %) and show He- and C-isotope values that are consistent with mantle sources (Minissale et al., 2017).

In summary, the North Abaya geothermal area (Fig. 2) is a zone of recent faulting and volcanism, with evidence for a mature geothermal system (stable over several decades, c.f.

Chernet, 2011). The circulating fluids are of meteoric origin undergoing significant water-rock interaction and flushed by magmatic gases (Minissale et al., 2017). Despite this, the subsurface architecture of the geothermal system and the relationship between faulting, magmatism and hydrology at Abaya remain poorly understood. Our work addresses this question via remote sensing and high spatial resolution soil gas surveys which provide important insights into the magmatic-hydrothermal system and allow us to pinpoint the most permeable structures that could be targeted for geothermal drilling (Jolie et al., 2019).

3. Methods

3.1 Remote sensing

To map volcanic landforms and tectonic structures in North Abaya we used a 12.5 m digital elevation model (DEM) from the Japanese ALOS satellite (ALOS PALSAR). These data were combined with previous fault data bases of Agostini et al. (2011) and Corti et al. (2013). Ground deformation is frequently observed at geothermal sites in Ethiopia (e.g., Biggs et al., 2011; Hutchison et al., 2016; Birhanu et al., 2018; Lloyd et al., 2018) and for Abaya we evaluated this using satellite radar interferometry (InSAR). Recently, Albino and Biggs (2020) used Sentinel-1 data provided by the European Space Agency (ESA) to generate an InSAR time series along the entire EARS for the period 2015–2020. Here we explore a subset of the data from North Abaya and for full details of the processing please the reader should refer to Albino and Biggs, (2020).

3.2 Soil CO_2 flux and temperature surveys

Soil CO_2 flux and temperature were measured in January-February 2019. The objectives of our survey were firstly, to transect major rift faults in the SE of the study area and secondly, to generate detailed maps of soil degassing along the West Abaya graben fault and the flank of the Salewa Dore-Hako rhyolitic complex (the main volcanic edifice in the study area, Fig. 2a). The typical spatial resolution of our sampling was 50 m and in total 757 measurements were made. CO_2 flux was measured via the accumulation chamber technique (Parkinson, 1981; Chiodini et al, 1998). We used a Westsystems flux meter with an inbuilt LICOR-LI820 CO_2 concentration sensor and the flux measurement was based on the rate of CO_2 increase in the chamber over a 2-minute measurement period. Repeat measurements were typically within 10–25 % and showed better precision in high flux zones. These values are similar to previous geothermal studies (e.g. Hutchison et al., 2015) and are typical of the instrument reproducibility and natural variations in emission rates (Chiodini et al., 1998; Carapezza and Granieri, 2004; Giammanco et al., 2007; Viveiros et al., 2010).

At each station we measured soil temperature using a Digi-Sense Type K thermocouple probe and an Oakton Temp 10 Thermocouple Thermometer inserted to 50 cm soil depth. To create the measurement hole, we used a sledgehammer to drive a 50 cm metal bar into the ground before inserting the thermocouple. Note that in all cases CO_2 flux was measured before the 50 cm hole was made and since penetration through the soil causes frictional heat, the probe was left in place until a stable temperature reading was obtained. In some locations the 50 cm depth could not be reached (due to stones or bedrock) and so the depth of the probe was recorded as well as the temperature (Table S1).

To produce maps of CO_2 flux and temperature we used a sequential Gaussian simulation (sGs) method (Cardellini et al., 2003). These methods allow the user to undertake 100's of realisations of the survey grid and are particularly useful for CO_2 because they constrain the uncertainty in the total flux. sGs methods require a high data sampling density and hence were only attempted on the Western flank of the Abaya Graben and the flank of the Salewa Dore-Hako rhyolitic complex. 300 sGs were performed using the sgsim simulation tool (Deutsch and Journel, 1998) in the Stanford Geostatistical Modelling Software (SGeMS) package (Remy et al, 2009). To generate maps, we calculated the arithmetic mean of each individual cell across all simulations and for CO_2 we calculated the total flux of each simulation and used this to compute the mean and standard deviation of all simulations and assess total CO_2 emission and its uncertainty.

3.3 Gas sampling and geochemical analysis

3.3.1 Bulk gas chemistry and carbon isotopes

Dry gas samples from gas-rich springs and fumaroles gas were collected in 9 ml pre-evacuated tubes. These samples were then analysed for bulk chemistry and C isotopes ($\delta^{13}C$) at the Department of Earth and Planetary Sciences at University of New Mexico (USA). Gas chromatography (GC) and quadrupole mass spectrometry (QMS) were used to measure CH_4-CO_2-H_2-CO and Ar-He-N_2-O_2 concentrations, respectively. Experimental errors for the GC and the QMS are <2 and < 1% respectively (Lee et al., 2017). Due to collection of samples in glass vials with rubber septa, He and H_2 are likely to rapidly diffuse out of the vials and results for these gas species are not representative of the composition of the gas discharge.

Samples with the highest concentrations of CO_2 were selected for $\delta^{13}C$ analysis using a Thermo Scientific Delta Ray Infrared Spectrometer. The samples were diluted using the capillary dilution system provided by the manufacturer and introduced to the inlet of the instrument through a needle and capillary. In order to compensate for pressure decrease during analyses, a pure N_2 gas was connected to the vial. Calibration was performed prior to and following the analyses with a commercially available calibration gas and all CO_2-$\delta^{13}C$ measurements are shown in delta notation as per mil values (δ ‰) relative to Vienna Pee Dee belemnite (VPDB). Our measurements are characterized by a $\delta^{13}C$ standard error of ±0.1‰.

3.3.2 Helium isotopes

For helium isotope measurements gases were collected in Cu-tubes from moderate to high temperature (60–95 °C) bubbling springs and fumaroles. At each locality, samples were collected using (3/8-inch) Cu-tubes connected at one end with Tygon tubing fitted with an inverted funnel, which was inserted into the source of gas manifestation (e.g., Weiss, 1968; Kennedy et al., 1985). The other end of copper tube was fitted with a second section of Tygon tubing, a second copper tube and a third section of Tygon tubing, which was submerged in water to ensure a one-way flow of gas through the sampling apparatus, thus minimizing air contamination. Approximately 1–2 hours were taken to flush the entire sampling apparatus before sealing both ends of the copper tubes using specially designed stainless-steel clamps that create a cold-weld in the Cu-tubing, thus sealing sample gas inside of the tube for transport to the laboratory.

Noble gas isotope analysis was conducted using a dual mass spectrometer setup, interfaced to a dedicated extraction and purification system at the University of Oxford (Barry et al., 2016). In brief, gases collected in Cu-tubes were transferred to the extraction and purification line where reactive gases were removed by exposing gases to a titanium sponge held at 950°C. The titanium sponge was cooled for 15 minutes to room temperature before gases were expanded to a dual hot (SAES GP-50) and cold (SAES NP-10) getter system, held at 250°C and room temperature, respectively. A small aliquot of gases was segregated for preliminary analysis on a quadrupole mass spectrometer. He and Ne isotopes were then concentrated using a series of cryogenic traps; heavy noble gases (Ar-Kr-Xe) were frozen down at 15 K on a stainless-steel finger and the He and Ne were frozen down at 19 K on a cold finger filled with charcoal. The temperature on the charcoal finger was then raised to 34 K to release only He, which was inlet into a Helix SFT mass spectrometer. Following He analysis, the temperature on the charcoal cryogenic trap was raised to 90 K to release Ne, which was inlet into an ARGUS VI mass spectrometer. Uncertainties on helium isotopes and He/Ne values are less than 3 %.

4. Results

4.1 Tectonics and recent volcanism

Fault structures in the North Abaya study area are shown in Figure 2. We mapped three major graben structures (the Salewa Dore-Hako graben, the Abaya graben and Chewkare graben) as well as regional faults that define an overall NNE-SSW trend. Graben bounding faults show the greatest displacement (Fig. 2c) with the West Abaya graben fault marked by the largest vertical offset of ~110 m. Overall, the North Abaya faults displays a right-stepping *en echelon* pattern (Corti et al., 2013) which leads to various intersecting fault zones. This is particularly well developed at the southern end of the West Abaya graben fault where a ~100 m high wedge-shaped horst block is observed (Fig. 2b). We refer to this area as the Abaya horst and a field photograph from the west of this structure looking south shows that this is a site of fumarolic activity where hydrothermal upwelling has led to surface alteration and the formation of bright red clays. On the ground these fumaroles display an WNW-ESE alignment which suggests these vents are linked to WNW-ESE structures orthogonal to the West Abaya graben fault. Importantly we found field evidence for the existence of such faults along the shore of Lake Abaya where a WNW-ESE fault with a throw of 2–3 m was observed (Fig. 3b). We suggest that although major NNE-SSW rift-aligned tectonic faults accommodate the bulk of extension their *en echelon* fabric creates numerous intersecting fault sets that may develop into highly fractured ‘gridded’ fault zones (as seen in the Abaya horst).

Our mapping of volcanic vents shows that these are mainly located in the Salewa Dore-Hako graben (in agreement with previous studies, Corti et al., 2013). Mafic scoria cones define a ~20 km long NNE-SSW trend, while silicic vents are focused at the ~5 km long ~N-S oriented Salewa Dore-Hako rhyolitic complex which comprises overlapping obsidian coulees. The overall NNE-SSW alignment of the mafic vents suggest a feeder dyke of similar orientation (Corti et al., 2013), while the more chemically evolved silicic volcanism is indicative of an upper crustal (~5 km deep) magma reservoir as observed elsewhere in the rift (e.g., Aluto, Hutchison et al., 2016; Gleeson et al., 2017, Iddon et al., 2019). Fumaroles are observed at the Salewa Dore-Hako rhyolitic complex, but they are much weaker that than the activity observed along the West Abaya graben fault (Fig. 3a).

4.2 Ground deformation

The results of a 2015–2020 Sentinel-1 InSAR survey for the North Abaya region are shown in Figure 4. The map shows the mean line of sight velocity (in cm yr^{-1}) relative to a reference area that is located >30 km east of the study area and well distanced from any volcanic or tectonic features. Deformation rates in the North Abaya geothermal area are on the order of 0 to –0.5 cm yr^{-1}. Albino et al. (2022) investigated limits of detection in this Sentinel-1 time series and demonstrated that linear deformation rates must be greater than 0.5 cm yr^{-1} to be detected over this 5-year period. At North Abaya, deformation rates (Fig. 4) clearly fall below the limits of detection and are negligible when compared to uplift/subsidence signals that typify other East African volcanoes that host geothermal resources (typically >2 cm yr^{-1}, Albino and Biggs, 2020). Thus, our data show that there was no significant deformation in the North Abaya study area during the 2015–2020 period.

4.3 CO_2 degassing and soil temperatures

Maps of CO_2 flux and soil temperatures are shown in Figures 5 and 6, respectively. CO_2 flux ranged from 0.2 to 6020 g m^{-2} d^{-1} and showed elevated values along the West Abaya graben fault, with the highest values observed around the northern wedge of the Abaya horst. A few elevated CO_2 flux values were observed at the Salewa Dore-Hako rhyolitic complex and along graben bounding faults, but within the centre of the grabens fluxes were low (Fig. 5). Soil temperatures (Fig. 6) were between 18.3 and 98.5 ºC. They also show high values associated with the West Abaya graben fault but unlike CO_2 elevated temperatures were only observed at the northern wedge of the Abaya horst rather than along the length of the fault. Temperatures were low (<45 ºC) on the Salewa Dore-Hako rhyolitic complex except for some weak fumaroles located on the top of the complex.

To evaluate the existence of different CO_2 and temperature sources we used the graphical statistical analysis method (GSA) described by Chiodini et al. (1998). This method involves visual analysis of log-probability plots (Fig. 7), and it is expected that when data consist of a single log-normal population this will plot as a straight line, and when there are multiple log-normal populations these will plot as curves of overlapping populations defined by inflection points. Our CO_2 flux and soil temperature data show clear inflections points at values of 28.2 g m^{-2} d^{-1} and 40 ºC, respectively. We interpret these two populations as: 1) a magmatic-hydrothermal source (associated with high temperatures and high CO_2 flux) and 2) a background source (associated with low temperatures and low CO_2 flux, and most likely derived from biogenic and/or deep magmatic/mantle sources). In Figures 8 and 9 we show transects along and across the major faults and volcanic areas of the study area, and we use the upper value of the background population to help identify areas of significant magmatic-hydrothermal input.

Before looking at transects in detail it is important to point out two notable features of the background population. Firstly, while background CO_2 flux at North Abaya (0.2 to 28.2 g m^{-2} d^{-1}) is within the range of typical non-volcanically influenced soil (10–30 g m^{-2} d^{-1}, Mielnick and Dugas, 2000; Rey et al., 2002; Cardellini et al., 2003) it is higher and more variable than other sites in the MER (i.e. 0.5 to 6.0 g m^{-2} d^{-1} at 10–20 km distance from Aluto volcano, Hutchison et al., 2015). Secondly, within the background CO_2 flux population we noted minor inflections at 12.6 and 2.0 g m^{-2} d^{-1} (Fig. 7a). The first feature is explained by the fact that North Abaya is much more vegetated than the area surrounding Aluto (the former is adjacent to a large lake and within a major river catchment) and therefore the soil is richer in organic material and hence biogenic CO_2 flux is almost certainly higher. The second feature, regarding multiple minor inflections in the log-probability plot, suggests there may be several background CO_2 flux populations. Interestingly, some of the more elevated background values do appear to be associated with rift aligned faults (e.g., the red labelled fault in Fig. 9, C-C' shows a CO_2 flux 26 g m^{-2} d^{-1}). An explanation is that these faults sites have enhanced permeability and a greater deep magmatic/mantle CO_2 flux that is unrelated to any near surface volcanic-hydrothermal system. We did not collect C isotope samples for these different background sites and so we cannot be certain whether there is a stronger biogenic fingerprint at Abaya, and whether elevated background values associated with faults display a magmatic signature. For completeness we include these inflection points in the background population in Figure 8 and 9, and we emphasise that while the high temperature, high CO_2 flux magmatic-hydrothermal source is clearly defined there is undoubtedly a range of biogenic and deep mantle/magmatic CO_2 sources captured in the background population.

Given this broad categorisation of magmatic-hydrothermal and background populations we can take a more detailed look at spatial variations in soil CO_2 flux and temperature using transects (shown in map view in Figures 5 and 6, and as plots in Figures 8 and 9). Transect A-A'-A" shows CO_2 flux and temperature from south to north along the West Abaya graben fault (Figure 8). CO_2 flux is variable along the fault but shows highest values at the Abaya horst and a maximum value of 6020 g m^{-2} d^{-1} in the area ~500 m north of this structure. Maximum CO_2 flux values then show a general northward decrease to more typical background values. It is important to note that between ~1500 and ~2300 m along the profile we were unable to access the hanging wall of the fault because of surface water, and so the lack of high CO_2 in this area likely reflects a gap in sampling rather than a genuine decrease in CO_2 flux in this section of the fault. Soil temperature is also at highest values at the Abaya horst (up to 98.5 °C at the fumaroles in Fig. 3a). Notably, between 2300 and 3500 m there is elevated CO_2 but only a few temperatures >40 °C. This demonstrates that CO_2 flux and soil temperature are not always correlated and therefore CO_2 and hydrothermal steam do not always travel together.

Transect B-B' includes several fault structures in the Salewa Dore-Hako graben and then rises eastwards on the flank of the Salewa Dore-Hako rhyolitic complex (Fig. 9). No significant temperature anomalies were detected along this profile. CO_2 flux showed no evidence for elevated values across the intra-graben faults but did show several elevated values up to 176 g m^{-2} d^{-1} on the volcanic complex. These maximum CO_2 values are an order of magnitude lower than those obtained on the West Abaya graben fault (Figure 8). The elevated CO_2 flux on the volcanic complex appears to be localized (Fig. 5) and does not show an obvious NNE-SSW (fault controlled) trend, arguing against a tectonic control on CO_2 degassing. Instead, there appears to be a closer relationship between CO_2 flux and elevation with peak values in CO_2 approximately centred on a topographic high.

Transect C-C' covers the eastern escarpment of the Salewa Dore-Hako graben as well as a regional fault to the west of this (Fig. 5). Although the vertical offset for these faults are broadly comparable (~20 m and ~15 m for the graben fault and regional fault, respectively) there is a marked contrast in their CO_2 emission with the regional fault showing subtle variation in background values and the graben fault showing a ~400 m wide zones of elevated values (up to 58 g m^{-2} d^{-1}). This finding suggests that the graben bounding faults provide more permeable conduits for deeper magmatic-hydrothermal gases.

Our high-density survey grid along the West Abaya graben fault and the flank of the Salewa Dore-Hako rhyolitic complex allowed us to construct maps of CO_2 flux and temperature using sGs methods (Fig. 10). The results mirror the trends in the underlying data (i.e., Figures 5 and 6) and clearly indicate highest CO_2 flux and temperatures along the West Abaya graben fault particularly at the wedge of the Abaya graben. For CO_2 we calculated the total flux (shown as mean ± standard deviation) and the key finding is that while the two survey sites cover a similar area (3.8 and 3.9 km^2), the total flux along the West Abaya graben fault is 294 ± 71 t d^{-1} which is 10× greater than on the flank rhyolitic complex (29 ± 3 t d^{-1}).

4.4 Gas chemistry

Compositions of gas samples are shown in Table 1. Our samples mainly contain N_2, O_2 and CO_2 and represent air that has been flushed by gases of magmatic-hydrothermal origin. Those samples that are rich in CO_2 (up to 30–36 %) represent the most pristine magmatic gas samples.

Minor gas species include He, H_2, Ar, CH_4 and CO, which originate from a combination of atmospheric and magmatic sources, as well as reducing reactions in the hydrothermal reservoir (i.e., CH_4 and CO, Agusto et al., 2013; Tassi et al., 2013).

New carbon isotope ($\delta^{13}C$) data for CO_2 from Abaya are compared to previous measurements from volcanic-hydrothermal systems across the East African Rift in Figure 11a. Our Abaya data show values from –6.4 to –3.8 ‰ which are almost identical to previous $\delta^{13}C$-CO_2 made at the same localities by Minissale et al. (2017). Plotting the isotope data versus the reciprocal of CO_2 concentration in the samples reveal a crude triangular array that is usually interpreted as mixing between air, biogenic and magmatic CO_2 (Fig. 11a, where end-member $\delta^{13}C$ values come from Gerlach and Taylor, 1990; Javoy and Pineau, 1991; Macpherson and Mattey, 1994; Sano and Marty, 1995; Darling et al., 1995; Tedesco et al., 2010; Cheng, 1996 and Chiodini et al., 2008). The Abaya gas samples were all extracted from fumarole vents and are clearly focused on the magmatic endmember. This contrasts with previous surveys of the Magadi-Natron rift basin (Lee et al., 2016; Muirhead et al., 2020) and the Aluto geothermal system (Hutchison et al., 2016) which sampled soil gas at both fumarolic and non-fumarolic sites and therefore showed a wider spread of both $\delta^{13}C$ and CO_2 concentration. Focusing on the magmatic endmember (Fig. 11b) reveals that in the most pristine magmatic gas samples there is overlap between Abaya and Aluto (currently Ethiopia's only developed geothermal site).

Helium isotopes are shown in Figure 11c. The X-value gives the $^{4}He/^{20}Ne$ ratio of the sample relative to that measured in air and therefore gives an indication of how much air has been entrained into the sample. X-values close to 1 are air-dominated, and for our samples X-values are 6.3 and 12.8 implying limited air incorporation. Using the X-values we correct our samples for the presence of atmospheric He isotope values (after Hilton, 1996) and this yields He isotope values (R_C/R_A) values of 4.4 (Table 1). Again, these values are similar to previous measurements of North Abaya by Minissale et al. (2017) who found R_C/R_A values of 4.5 to 7.5 at similar locations along the West Abaya graben fault. Our helium isotopic compositions are lower than MORB-like values (typically 8 ± 1 Graham, 2002) and show close resemblance to a sub-continental lithospheric mantle (SCLM) source (Gautheron and Moreira, 2002; Bräuer et al., 2016; Gilfillan and Ballentine 2018, Fig. 11c).

5. Discussion

5.1 Controls on volcanism, hydrothermal fluids and degassing

The North Abaya region is dominated by NNE-SSW trending *en echelon* normal faults (Corti et al., 2013) which have an overall horst-graben structure (Fig. 2). The Abaya and Chewkare grabens comprise the rift floor while the Salewa Dore-Hako graben accommodates a transition from the rift shoulder towards the rift floor. The most significant deformation is accommodated on the graben bounding faults and in particular the West Abaya graben fault which accommodates ~110 m of vertical offset and represents the major structure in the study area. The region either side of a fault plane is referred to as the damage zone and is usually represented by highly fractured and permeable lithologies (Bense et al., 2013). Importantly, fault damage zone width increases with fault displacement (Knott et al., 1996; Sperrevik et al., 2002; Faulkner et al., 2011; Choi et al., 2016). Given that the West Abaya graben fault shows the greatest displacement it is also expected to represent the most permeable zone, and this can explain why gas and fluid upflow is concentrated here (as evidenced by fumarolic activity, hot springs and the elevated ground temperatures and CO_2 flux, Figs, 3a,5,6). Although the displacement and geothermal activity on the West Abaya graben fault exceeds all other faults, we note that other graben bounding faults do show elevated CO_2 flux (see transect C-C' in Figure 9). While the CO_2 flux is much lower it does suggest that the graben bounding faults are key pathways for CO_2 release and that they are more permeable and/or deeper penetrating than the regional intra-graben faults.

Volcanism in the study area is mainly restricted to the Salewa Dore-Hako graben (Fig. 2a). Mafic scoria cones span a ~20 km long NNE-SSW oriented trend, while silicic vents are restricted to the Salewa Dore-Hako rhyolitic edifice in the centre of this segment. The elongate trend suggests feeder dyke(s) beneath the basin, in agreement with vent elongation (Corti et al., 2013). From our CO_2 flux observations, we identified that graben bounding faults act as high permeability zones. However, volcanic vents are not aligned to these faults and are instead found scattered across the centre of the graben. Thus, graben bounding faults do not appear to represent preferential structures for magma ascent and our data suggest that dykes are emplaced in the centre of the Salewa Dore-Hako graben and that regional intra graben faults direct magma toward the surface (c.f. Corti et al., 2013).

As noted above the West Abaya graben fault shows intense surface alteration (Fig. 3a) and the most elevated ground temperatures and CO_2 flux in the study area (Figs 5, 6). High resolution topography (Fig. 2b) shows that this margin of the graben is typified by multiple faults which interact and intersect and that the highest ground temperatures are focused in a wedge shaped zone at the tip of the Abaya horst. Intersecting faults are known to enhance permeability and fluid circulation (Curewitz and Karson, 1997; Person et al., 2012) and we suggest that these interactions at the Abaya horst, as well as the large damage zone of the West Abaya graben fault explain why this is an area of intense hydrothermal upflow.

A further feature of the Abya horst is the occurrence of ~W-E oriented faults (Fig. 3a). Although these features have minor offsets (2–3 m) compared to the NNE-SSW aligned faults (10–100 m), it is likely that they also enhance the permeability and direct fluid flow because fumaroles at the tip of the Abaya horst show a WNW-ESE alignment (orthogonal to the trend of the West Abaya graben fault). Cross rift (~W-E) oriented structures have been documented at many volcanic systems throughout the EARS (Acocella et al., 2003; Robertson et al., 2016; Llyod et al., 2018; Hunt et al., 2019), and while we cannot ascertain the extent of these structures at Abaya, they do appear to play an important role directing fluids and gas towards the near surface. In summary, our study reveals that the West Abaya graben fault controls the main upflow of hydrothermal fluids and gas from depth, and that intersecting faults enhance the permeability of this zone concentrating fluids around the wedge tip of the Abaya horst.

At the Abaya horst we see high values of both CO_2 flux (2000 g m^{-2} d^{-1}) and ground temperature (> 90 °C), but it should be noted that this is not the case along the entire length of the West Abaya graben fault. For example, around A' in our transect in Figure 8 CO_2 is significantly elevated while temperatures are only just above background values of 40 ºC. This indicates that CO_2 and steam transport are decoupled, and it is explained by the fact that steam, which usually travels together with CO_2, has condensed to water during transport. There are several springs and surface water bodies in the vicinity of A', adjacent to the West Abaya graben fault. Our hypothesis is that steam ascending along this section of the fault intersects groundwater and condenses (i.e., when its temperature drops below 100 ºC, Fridriksson et al., 2006). CO_2 condenses at much lower temperatures (−78.5 °C) and is therefore unaffected by groundwater interactions.

CO_2 flux is also elevated above background values at a few localities on the Salewa Dore-Hako rhyolitic centre and the highest values were associated with steaming ground (with temperatures of 50 ºC). Our study mainly covered the SW flank of the rhyolitic centre and although we also conducted transects over several rift-aligned tectonic faults in the vicinity of the edifice, none show elevated CO_2 flux or ground temperatures (Fig. 9, B-B'). Previous work on Aluto volcano in the CMER (Hutchison et al., 2015) demonstrated the importance of localized permeability variations when trying to interpret diffuse CO_2 degassing. These localised variations may be associated with: 1) changes in the surface lithology (Pantaleo and Walter, 2013), for example, where there are differences in permeability between dense obsidian lavas and unconsolidated pumice deposits, and 2) topographic controls on the stress field, where differences in surface loading focus permeable pathways towards topographic highs (Schöpa et al., 2011). At Aluto, high CO_2 flux values (100–1000 g m^{-2} d^{-1}) were often observed at topographic highs associated with piles of young volcanic deposits and indicated that the topography-induced stress field played a role focusing fluid pathways toward morphological crests (Hutchison et al., 2015). Our transects of the Salewa Dore-Hako rhyolitic centre show similar correspondence between topography and CO_2 flux, and this leads us to infer a topographic control on the near-surface stress field. Our interpretation is that, like Aluto, there may be deep penetrating volcanic and/or tectonic structures which act as the main conduit of gas from depth, but once these gases enter the pile of unconsolidated volcanic material the permeability pathways are mainly controlled by the topographic loading, and this ultimately determines the surface expression of gas emission.

5.2 Volcanic gas emissions: origin and magnitude

The bulk gases collected from fumaroles (in glass vials) are mainly dominated by N_2 and O_2 and represent air mixed with variable amounts of CO_2 (up to 36 mol. %). When we consider various sources for the CO_2 (Fig. 11a), it becomes evident that their high CO_2 concentrations as well as $\delta^{13}C$ values of –6.4 to –3.8 ‰, require a magmatic origin for the CO_2. This is in good agreement with the findings of Minissale et al. (2017) who reported an almost identical range of CO_2- $\delta^{13}C$ from Abaya (Fig. 11b) and concluded a mantle-derived magmatic origin.

He isotope samples provide additional insights into the origin of gases. New air-corrected He isotope ($^3He/^4He$) measurements range from 3.8 to 4.1 R_A. These values are lower than previously published values from Minissale et al. (2017), who observed a range of 4.4 to 7.5 R_A for all Abaya samples (Fig. 11c). New data suggest that there may be a larger crustal contribution to gases collected in 2019. However, when taken together, He isotope values from the region overlap with canonical range of MORB (8 ± 1, Graham, 2002) and SCLM (6.1 ± 2.1, c.f. Gautheron and Moreira, 2002; Day et al., 2015; Bräuer et al., 2016; Gilfillan and Ballentine 2018). Although the highest $^3He/^4He$ values from Abaya do imply a MORB source we cannot exclude the possibility of SCLM contributions (given the overlapping values, Fig. 11c). Moreover, the fact that we see a range of values scattered to low $^3He/^4He$ is suggestive of radiogenic ^4He contributions from crustal sources (which have values of 0.02, Ozima and Podosek, 2002, Fig. 11c). Given that thermal fluids sampled along the West Abaya graben fault by Minissale et al. (2017) show clear evidence of water-rock interactions it is very likely that groundwaters from crustal sources contribute radiogenic ^4He. In short, the simplest explanation of the Abaya He isotope results is that they represent an upper mantle source with a crustal ^4He overprint. This explains the scattered values and indeed similar scenarios have been proposed in other areas of immature rifting further south in the EARS (e.g., the Magadi and Natron basins in Kenya and Tanzania, Lee et al., 2017). A final observation from Abaya $^3He/^4He$ measurements is that they are very different from the plume influenced measurements from Dallol in Afar (after Darrah et al., 2013, Fig. 11c). This supports geochemical evidence for a declining plume contribution SW along the MER (Rooney et al., 2012) and geophysical evidence for low-velocity anomalies focused beneath Afar and which have been linked to the African superplume (Bastow et al., 2010; Mulibo and

Nyblade, 2013; Ritsema et al., 1999, 2011). Helium isotope data clearly support the interpretation of the MER as transition zone between upper mantle and lithospheric sources in the south and plume-influenced mantle in the north towards Afar.

As noted in Section 5.2, the West Abaya graben fault and the intersecting fault network represent the deepest penetrating and most permeable area of North Abaya. CO_2 flux calculations support this and show that deep C emissions are focused along the West Abaya graben fault which emits ~300 t d^{-1} (10× the emissions from the flank of the rhyolitic complex, ~30 t d^{-1}, Fig. 10). Although there are only a few CO_2 flux measurements from elsewhere in the EARS it is evident that Abaya is an important C emitter; the flux is ~100× that of Longnot volcano in Kenya and ~3× that of the Oldoinyo Lengai summit area (Table 2). At Aluto volcano in the Central MER, Hutchison et al. (2015) measured CO_2 along a tectonic fault that dissects the volcanic edifice (Artu Jawe fault zone, Table 2) and found a CO_2 emission of ~60 t d^{-1} over an area of 0.8 km^2. Scaling up these calculations they calculated a total CO_2 flux from Aluto volcano of 250–500 t d^{-1}. This flux is of a similar magnitude to that of Abaya, although we emphasize that while CO_2 emissions at Aluto are associated with numerous volcano-tectonic faults spread over an area of ~150 km^2, the CO_2 released from Abaya is focused along a single tectonic fault. The CO_2 flux density also shows similar values between the West Abaya graben fault, the Artu Jawe fault zone on Aluto and other geothermal areas (e.g., Rotorua in New Zealand and Reykjanes geothermal area in Iceland, Table 2).

From a global perspective the CO_2 emission from Abaya compares with complexes such as Vesuvius (Italy), El Chichon (Mexico) and Tiede (Canary Islands), which all have active magmatic systems. More generally, estimates of CO_2 emissions from volcanoes with detectable SO_2 plumes (after Fischer et al., 2019 and Carn et al., 2017) suggest typical CO_2 fluxes between 100–300 kt yr^{-1}. Abaya's annual emission is ~110 kt yr^{-1}, which again underscores that even though Abaya does not represent a conventional volcanic edifice, the CO_2 emissions are comparable to the most active volcanic systems on Earth (Table 2). Taken together with the isotopic constraints (Fig. 11), this implies that an active magmatic system must underlie Abaya. CO_2 emissions from a volcanic system are mainly a function of the mass and C content of the degassing magmatic source, and the permeability of the fracture network (Burton et al., 2013).

While we cannot disentangle the role of source vs. permeability in controlling CO_2 emissions, the equivalence of Abaya and Aluto (in terms of total flux and flux density, Table 1) is notable because it implies similarities in terms of magmatic heat sources and subsurface permeabilities.

Given that Aluto represents a proven geothermal resource this finding should encourage further exploration at Abaya.

5.3 Architecture and geothermal potential

In Figure 12, we present a conceptual model of the North Abaya geothermal area based on our new measurements and the previous work of Chernet (2011), Corti et al. (2013) and Minissale et al. (2017). The heat for the geothermal field is sourced from magmatic intrusions and this is supported by the occurrence of recent, likely Holocene, volcanism in the area as well as our $\delta^{13}C$ and $^3He/^4He$ data as well as CO_2 flux constraints which indicate a magmatic system originating from an upper mantle source (Figs. 2, 11). Hydrothermal fluids sampled from thermal springs at Abaya show that springs have a dominantly Na-HCO_3 composition and indicate significant water-rock interaction. Importantly, their oxygen ($\delta^{18}O$) and hydrogen (δD) isotopes show a narrow range of values which parallel global and Addis Ababa meteoric water trends rather than evaporation trends that are observed in samples from Lake Abaya and the Bilate and Humasa rivers (Minissale et al., 2017). This clearly demonstrates that the deep fluids circulating beneath Abaya are meteoric in origin and are not linked to lakes or other surface water; their narrow $\delta^{18}O$-δD range imply a similar elevation, and we suggest that the rift margin to the west of the geothermal area provides the most likely source area. It is worth noting that this finding is comparable to Aluto volcano, where $\delta^{18}O$ measurements also reveal that despite proximity to major lakes, waters from the deep geothermal wells are meteoric in origin (>90%) and derived from rainfall on the rift margin (Darling et al., 1996; Rango et al., 2010).

The West Abaya graben fault is the main tectonic structure in the North Abaya area. Its large ~110 m vertical offset is far greater than any of the other faults and indicates a wide fault damage zone (Section 5.1) and enhanced permeability (evidenced by the highest values of soil temperature and CO_2 flux, Figs. 5–6). Field and remote sensing observations also indicate that this is a zone of fault intersection between the main graben bounding fault and other NNE-SSW regional faults (Fig. 2b), which has led to a complex *en echelon* fabric as well as small-scale E-W faults (Fig. 3b). In short, the West Abaya graben fault constitutes the main upflow zone from the deep geothermal reservoir, and the numerous fault intersections amplify permeability (c.f. Curewitz and Karson, 1997; Person et al., 2012) and concentrate fluid upflow at the tip of the Abaya horst (Fig. 6).

One of the key uncertainties with our model is the architecture of the deep magmatic heat source (Fig. 12). Although recent volcanism and hence magmatic intrusion appears to be focused in the Salewa Dore-Hako Graben, the main geothermal activity is offset from this and focused on the West Abaya graben fault (where there is no evidence of volcanic activity). We suggest the most likely heat source is unlikely to be associated with Salewa Dore-Hako rhyolitic complex because of its relatively small volume and location ~6 km north. We instead propose that the heat is sourced from a deeper mafic magma body (Fig. 12) due to the fact that volcanism south of the Salewa Dore-Hako (nearest to the West Abaya graben fault) is basaltic and indeed the formation of rhyolitic complexes necessitates large volumes of mafic intrusions (Hutchison et al., 2018). A similar setting to North Abaya may be the Butajira volcanic field in the CMER which shows linear clusters of scoria cones within a marginal graben structure (Hunt et al., 2020; Corti et al., 2018). Here, a magnetotelluric study by Hübert et al. (2018) showed that lines of scoria cones at the surface are offset from a deep conductive body at ~5-10 km depth which can be interpreted as mafic melt. This could be analogous to North Abaya where surface scoria cones may represent the surface expression of feeder dykes but not the deeper magmatic system.

To date, most studies of East African geothermal plays have focused on silicic caldera complexes (Gianelli and Teklemariam, 1993; Omenda, 1998; Hutchison et al., 2015; Hochstein et al., 2017). Magnetotellurics has proved particularly powerful at imaging geothermal resources, and at Aluto and Tulu Moye (Ethiopia) these data often suggest the presence of a shallow high conductivity clay cap layer overlying a low conductivity pressurised hydrothermal system (Samrock et al., 2015, 2018; Hübert et al., 2018). Magnetotellurics has been conducted at North Abaya by Reykjavik Geothermal and support the occurrence of a high conductivity clay cap rock at a depth of 0.5–2 km (Eysteinsson, pers. comm.). This is shown schematically on Figure 12 and we speculate that that the West Abaya graben fault provides the only major zone of permeability through this cap layer (hence why fumaroles, hot springs and degassing anomalies are largely restricted to this deep penetrating structure).

A final observation of the North Abaya geothermal area is that unlike the silicic volcanic complexes of Tulu Moye and Aluto there have been no episodes of ground deformation detected over a period spanning 1993 to 2020 (Biggs et al., 2011; Albino and Biggs, 2020, Albino et al., 2022; Fig. 4). At Tulu Moye, deformation has been linked to large scale pressurisation of the magmatic system, while at Aluto seasonal uplift-subsidence patterns related to rainfall and pore pressure changes of the hydrothermal system are superimposed on longer-term magmatic-hydrothermal pressurisation (Braddock et al., 2017; Hutchison et al., 2016). The fact that North Abaya displays neither of these trends demonstrates: 1) that there have been no detectable magmatic intrusions, and 2) that the geothermal reservoir does not respond to seasonal variations in rainfall. These data suggest that the mafic magmatic heat source beneath Abaya is less active and restless than the silicic mush systems of Tulu Moye and Aluto, it also suggests that the geothermal reservoir is potentially much larger than these other systems, or that timescales of groundwater flow between meteoric source and the heat source are much slower (such that seasonal variations in pore pressure are not observed). Ultimately, the lack of surface volcanism and ground deformation at Abaya stands in stark contrast with the restless silicic calderas elsewhere in the MER (Biggs et al., 2011; Albino and Biggs, 2020), and while further monitoring of Abaya is essential this does make it an attractive system for further exploration and development.

6. Conclusions and future opportunities

We have combined remote sensing, soil CO_2 and ground temperature surveys and gas chemistry analysis to build up a detailed understanding of the North Abaya geothermal system in the SMER. The main outcomes of our study are:

1) the North Abaya region displays a horst-graben morphology, and graben bounding faults represent the deepest penetrating, most permeable structures
2) soil CO_2 flux and temperatures reveal that the most permeable structure is the West Abaya graben fault, and that deep hydrothermal upflow is concentrated along this structure and into a zone of fault intersections
3) even though there is no surface volcanism along the West Abaya graben fault, gas emissions are ~300 t d^{-1} and comparable to average values from the world's sub-aerial volcanoes (e.g., Vesuvius, Teide, El Chichon, Table 2)
4) gas emissions require an active magmatic system, and new C- and He-isotopes suggest an upper mantle source (SCLM and/or MORB) that is overprinted by crustal ^4He additions

Our work presents the first detailed conceptual model of a fault-controlled magmatic geothermal resource in East Africa. The area is very promising for geothermal development and a key future step is to undertake geothermal drilling to test and refine our conceptual model (Fig. 12). The northern tip of the Abaya horst looks to be a particularly promising site, where ground temperature is highest, and permeability is enhanced by multiple intersecting faults.

Finally, compared to the active silicic caldera volcanoes that are generally seen as East Africa's best geothermal prospects, the West Abaya graben fault shows little evidence for recent volcanism. While there are still risks of volcanic and tectonic hazards in North Abaya area, and monitoring is to be encouraged, we suggest that fault-controlled geothermal plays, linked to deep mafic magma bodies sources, could represent safer and more sustainable prospects than silicic caldera volcanoes.

Acknowledgments

W. Hutchison is funded by a UKRI Future Leaders Fellowship (MR/S033505/1). E.R.D. Ogilvie was supported by a St Andrews Research Internship Scheme (StARIS) from the University of St Andrews.

Open Research

Data sets obtained from this research will be deposited on the St Andrews research portal (https://risweb.st-andrews.ac.uk/portal/) when the article is accepted. All data is available in the supporting information, tables, and/or figures for the purposes of peer review.

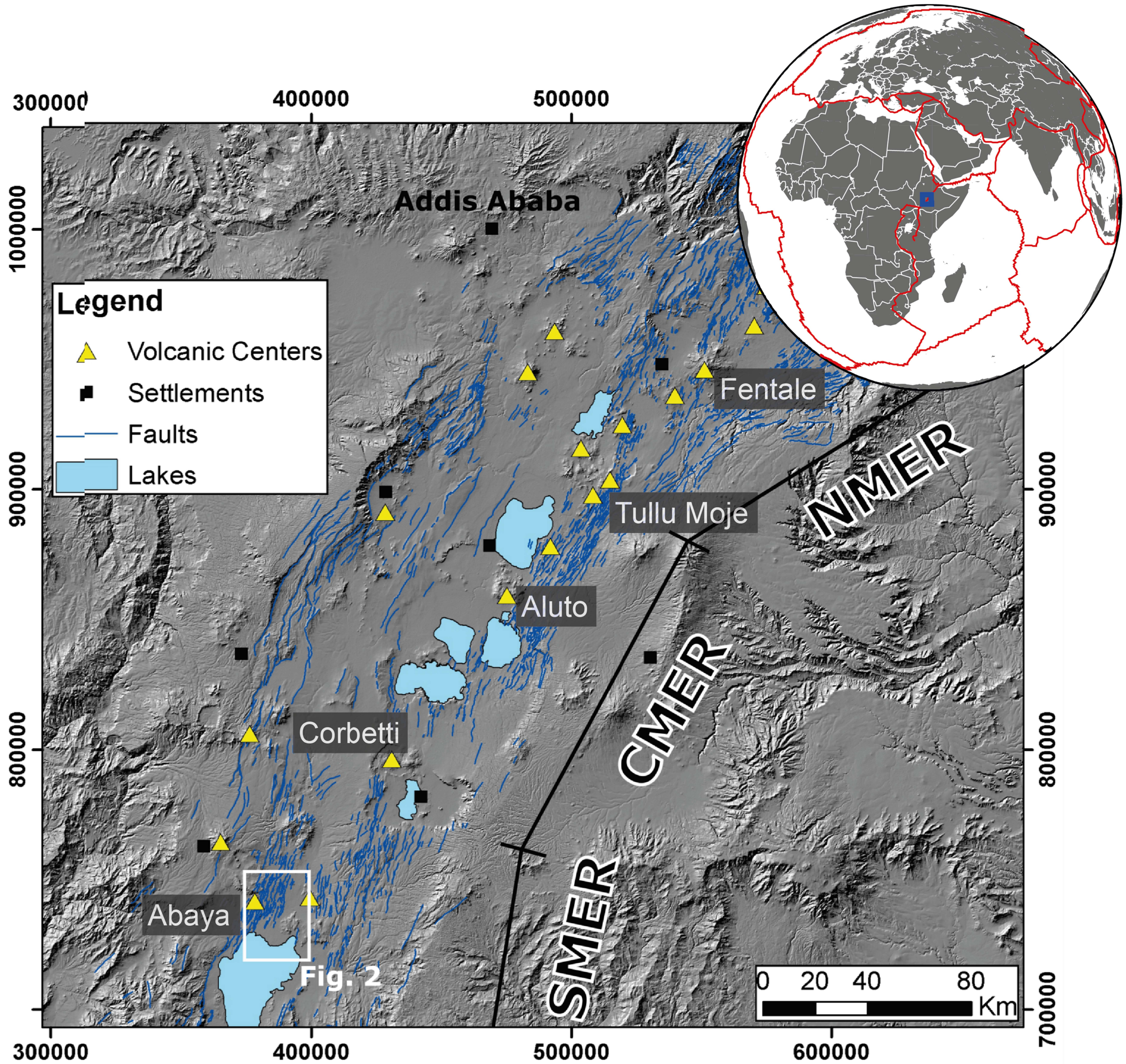

Figure 1. Hillshade Satellite Radar Topography Mission DEM of the Main Ethiopian Rift (MER). The MER is divided into northern, central and southern segments (NMER, CMER, SMER) and fault structures (modified after Agostini et al., 2011) are shown as blue lines. Volcanic centres are shown by yellow triangles, lakes are shaded blue and large settlements are shown by black squares. The Abaya volcanic field is located within the white rectangle. The globe inset shows major plate boundaries in red and the region covered by the DEM as a blue square.

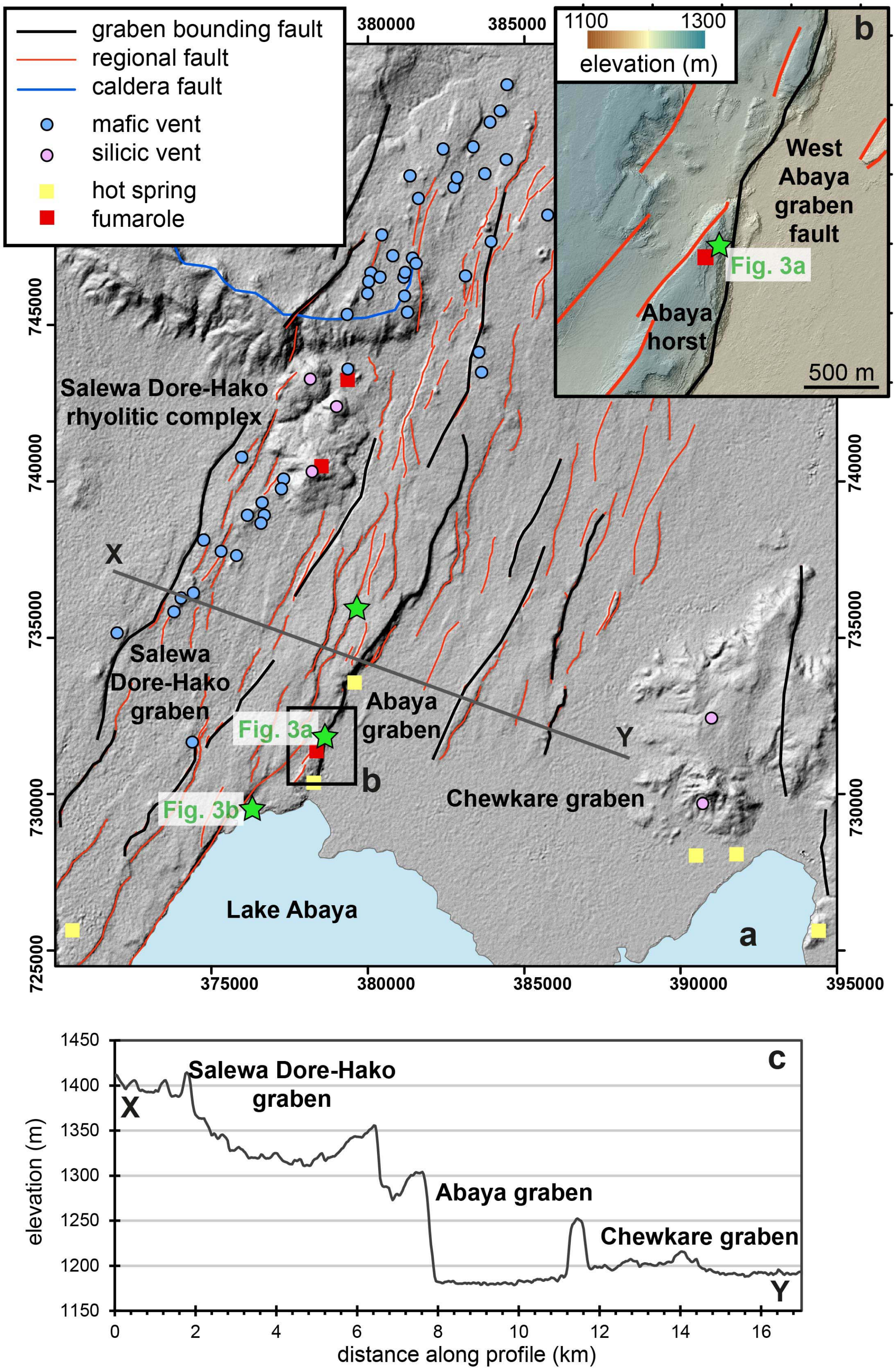

Figure 2. (a) Hillshade DEM of the North Abaya geothermal area. The main graben bounding faults are show by the black lines, while other NNE-SSW trending regional faults are shown in red. There are three prominent graben structures in the region: the Salewa Dore-

Hako, the Abaya and the Chewkare grabens. Mafic cones and silicic vents are shown by blue and pink circles, respectively. Hot springs and fumaroles are shown by yellow and red squares, respectively. The Salewa Dore-Hako rhyolitic complex is the largest volcanic edifice in the region. Green stars show the location of the photographs in Figure 3. **(b)** Shaded relief map showing the Abaya horst which is formed at the intersection of NNE-SSW trending regional faults and the main West Abaya graben fault**. (c)** Elevation cross-section of the Abaya area. The location of the section X-Y is shown in (a).

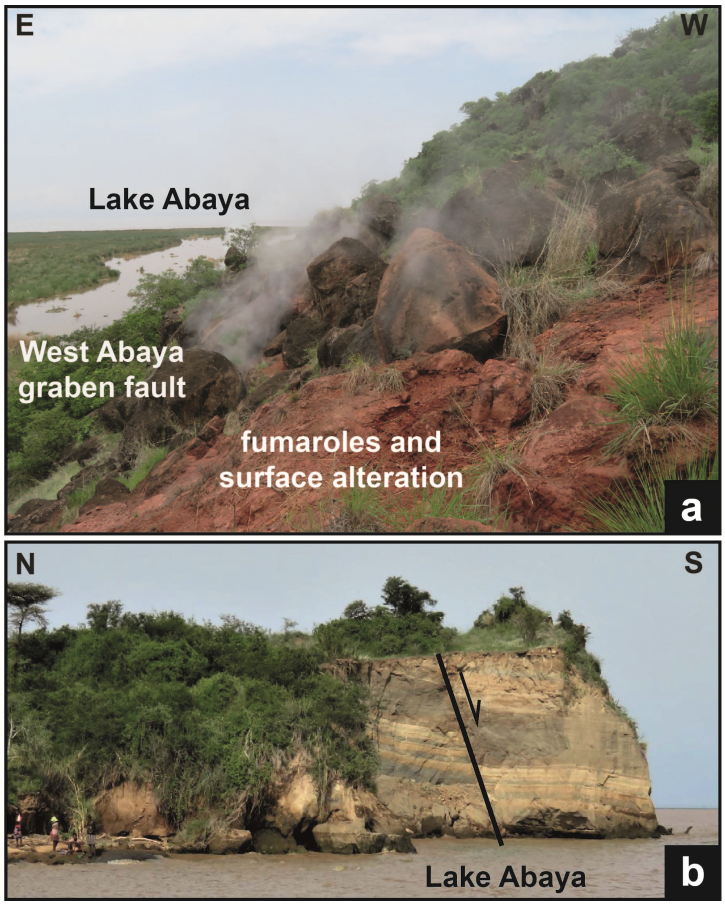

Figure 3: Field photographs. **(a)** Looking south along the escarpment of the West Abaya graben fault towards Lake Abaya. **(b)** Looking east towards the southern extent of the Abaya horst. A normal fault dipping towards the south is observed and has a throw of ~2–3 m (note people for scale at lower left of image).

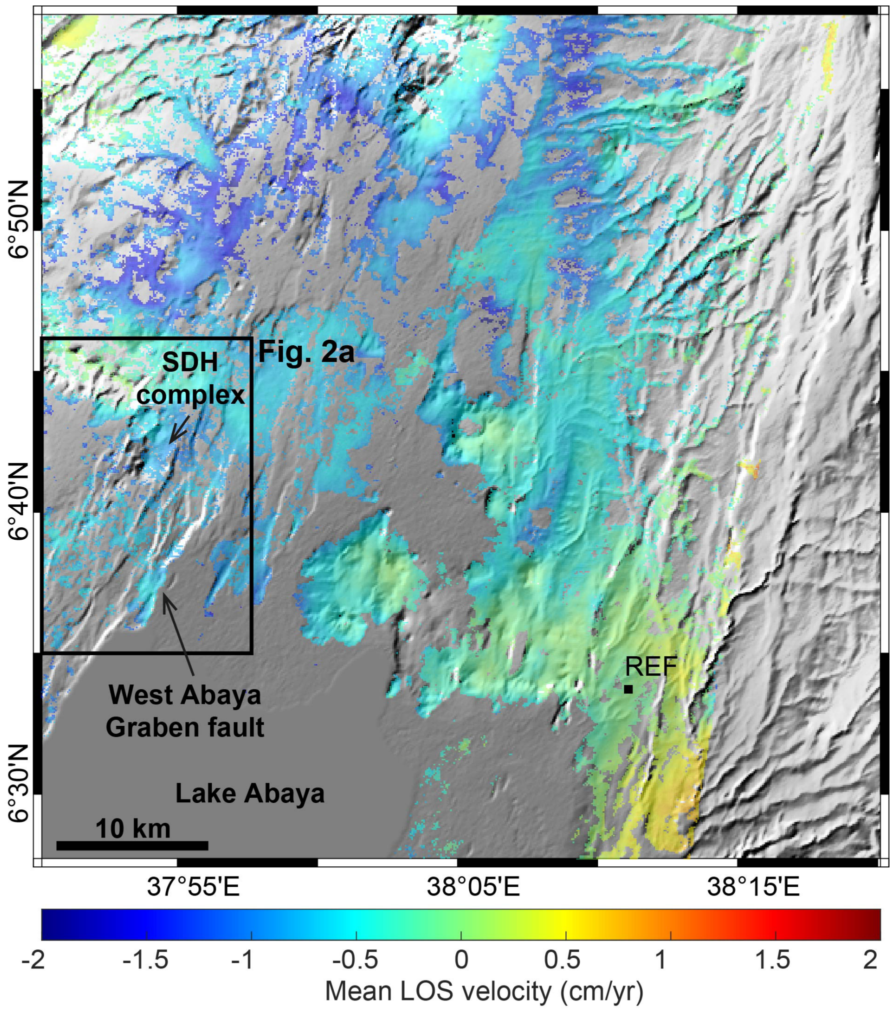

Figure 4: Ground deformation north of Lake Abaya during the period 2015-2020. The results are shown as mean line of sight velocity in cm/yr, relative to a representative reference area (labelled REF) that is well distanced from any volcanic and/or tectonic features (and assumed not to be deforming). Note that SDH indicates the Salewa Dore-Hako rhyolitic complex. Volcanic ground deformation usually results in uplift-subsidence of at least ±2 cm/yr. In this case no such deformation signals are detected.

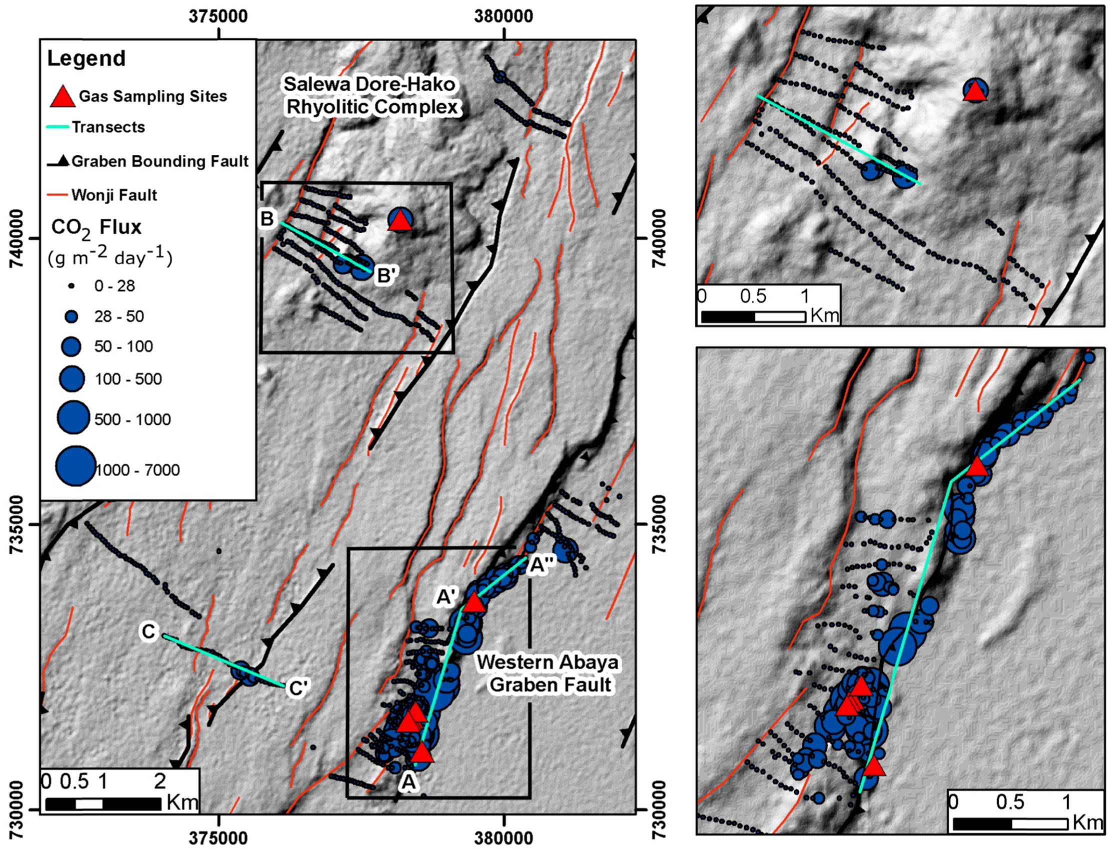

Figure 5. Hillshade DEM overlain with soil CO_2 flux values. The magnitude of the soil CO_2 flux corresponds to the size of the circle in accordance with the key on the left of the plot. Note that the smallest circles are typical of background, whereas larger circles are indicative of a volcanic-hydrothermal origin. Insets show CO_2 degassing at the Salewa Dore-Hako Rhyolitic Complex and West Abaya graben fault (in the upper and lower right-hand panels, respectively). Transects of the CO_2 degassing dataset are shown by the turquoise lines and are labelled A-A'-A'', B-B' and C-C'.

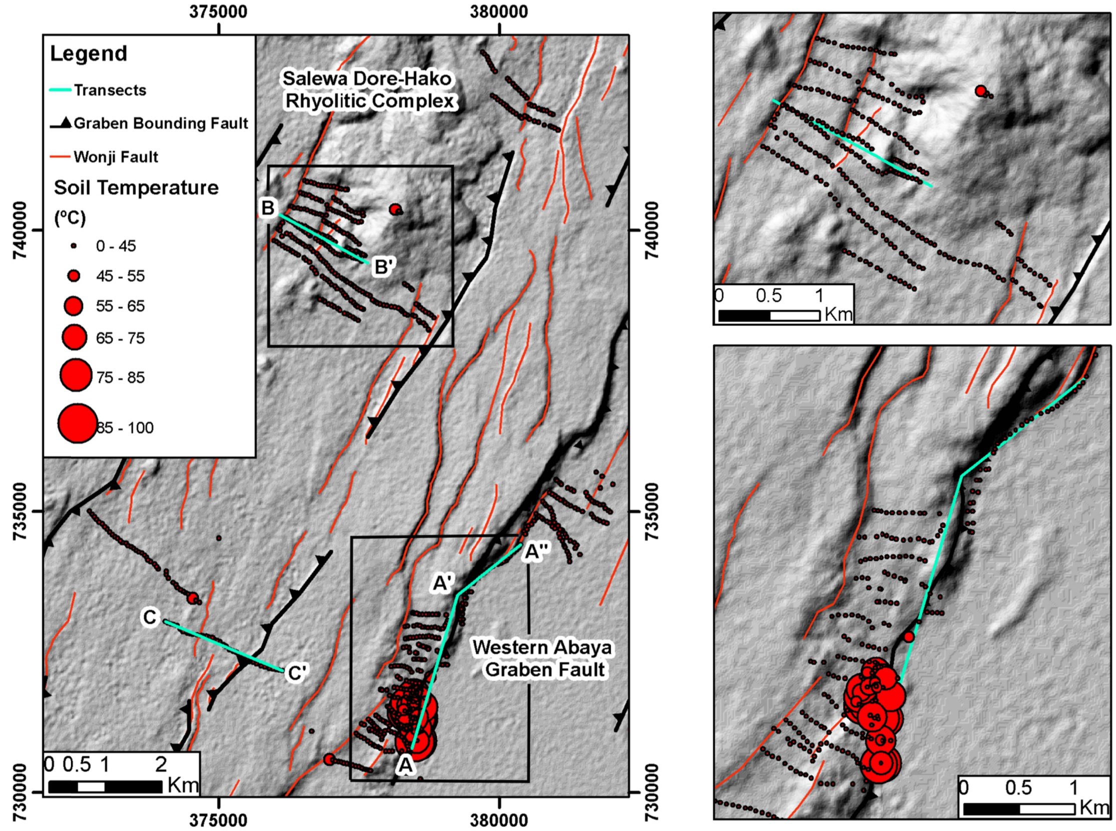

786
787
788 **Figure 6.** Hillshade DEM overlain with soil temperature values. The magnitude of the soil
789 temperature corresponds to the size of the circle in accordance with the key on the left of the
790 plot. Note that the smallest circles are typical of background, whereas larger circles are
791 indicative of upwelling hydrothermal. Insets show soil temperatures at the Salewa Dore-Hako
792 Rhyolitic Complex and West Abaya graben fault (in the upper and lower right-hand panels,
793 respectively). Transects of the dataset are shown by the turquoise lines and are labelled A-
794 A'-A", B-B' and C-C'.
795
796

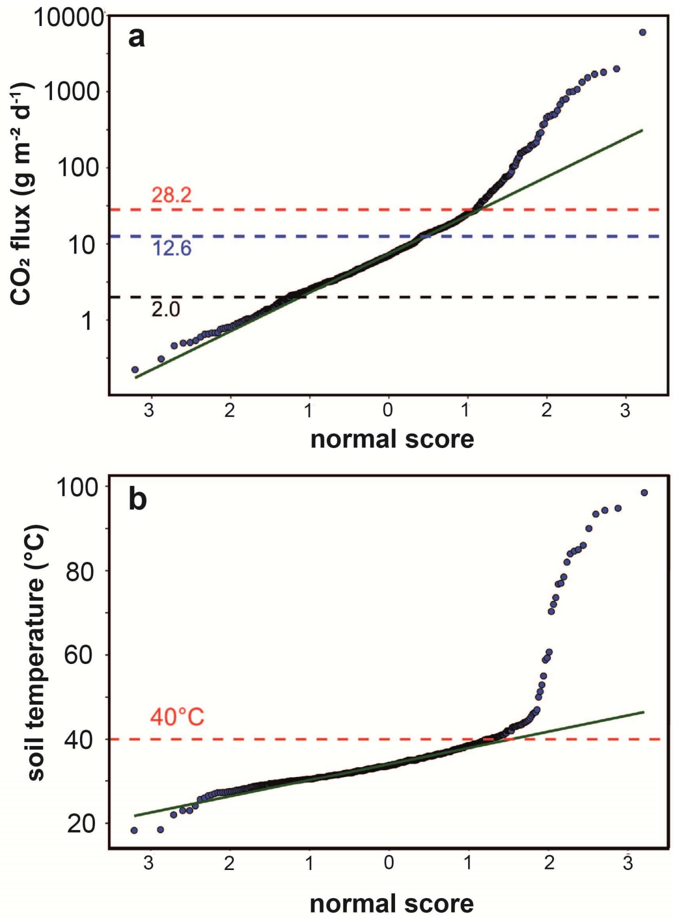

Figure 7. Probability plot of **(a)** soil CO_2 flux and **(b)** soil temperature. Inflection points in the probability plot are used to identify different background and volcanic-hydrothermal populations (see Chiodini et al., 1998). For temperature there is an obvious inflection at 40 °C which the upper limit of background values. For CO_2 the main inflection point is observed at 28.2 g m^{-2} d^{-1} and separates background from volcanic-hydrothermal populations. Minor inflections are observed in the background population, and we speculate that these could represent differences between faulted and non-faulted areas in regions where there is no underlying hydrothermal system (see Section 4.3 for discussion).

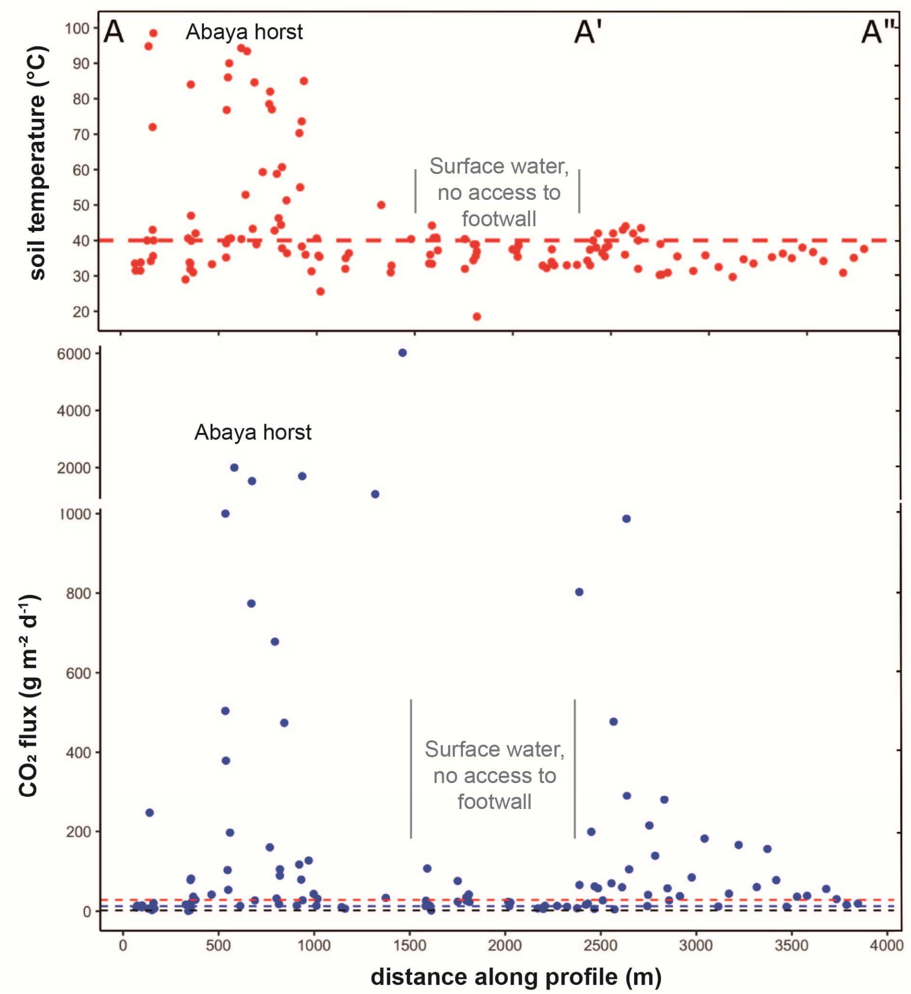

Figure 8. Soil temperature and CO_2 flux along the Western Abaya graben fault, A-A'-A" (in Fig. 5). Red horizontal lines denote the maximum value for background soil temperatures and CO_2 degassing, while the blue and black dashed lines represent minor inflections in background CO_2 populations referred to in Section 4.3. CO_2 flux and temperature are greatest around the wedge of the Abaya horst (i.e., towards the southern extent of the Western Abaya graben fault).

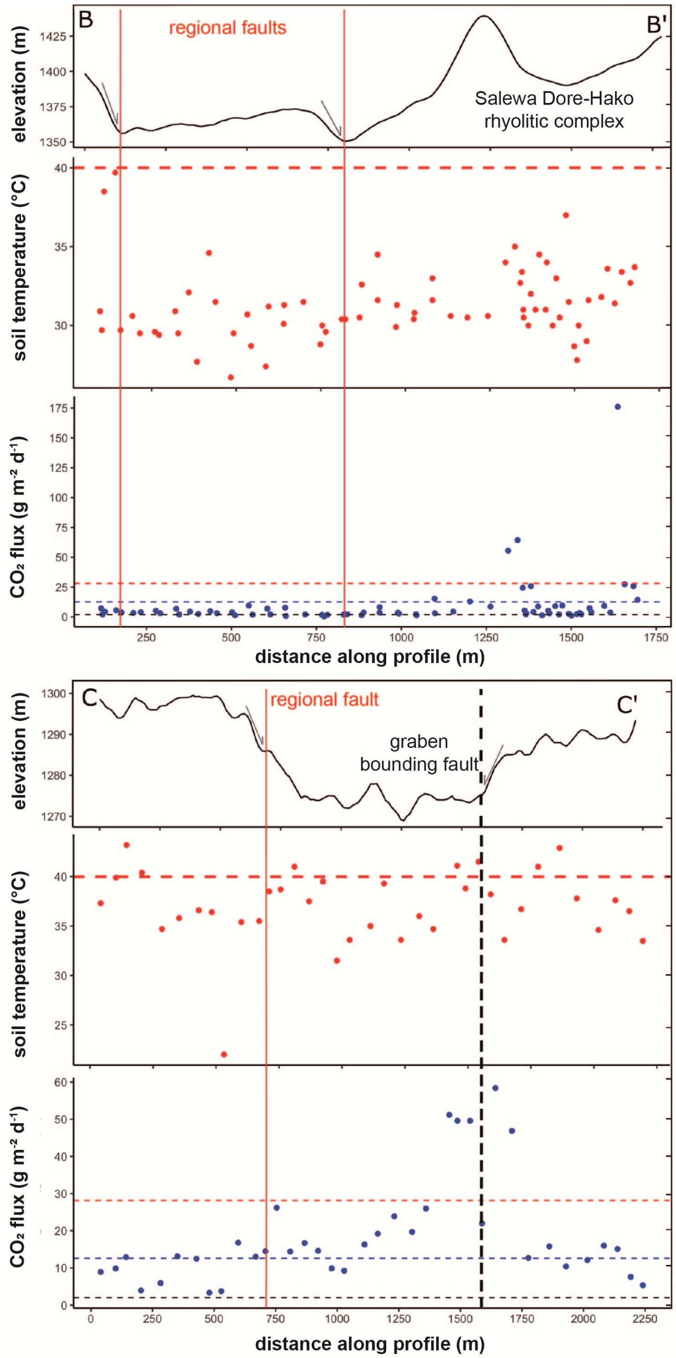

Figure 9. Transects of elevation, soil temperature and CO_2 flux across faults surrounding the Salewa Dore-Hako rhyolitic complex (B-B') and the eastern boundary of the Salewa Dore-Hako graben (C-C'). The vertical, black-dashed line represents the graben boundary fault while the red lines indicate mapped regional faults. Red horizontal lines denote the maximum value for background soil temperatures and CO_2 degassing, while the blue and black dashed lines represent minor inflections in background CO_2 populations referred to in Section 4.3.

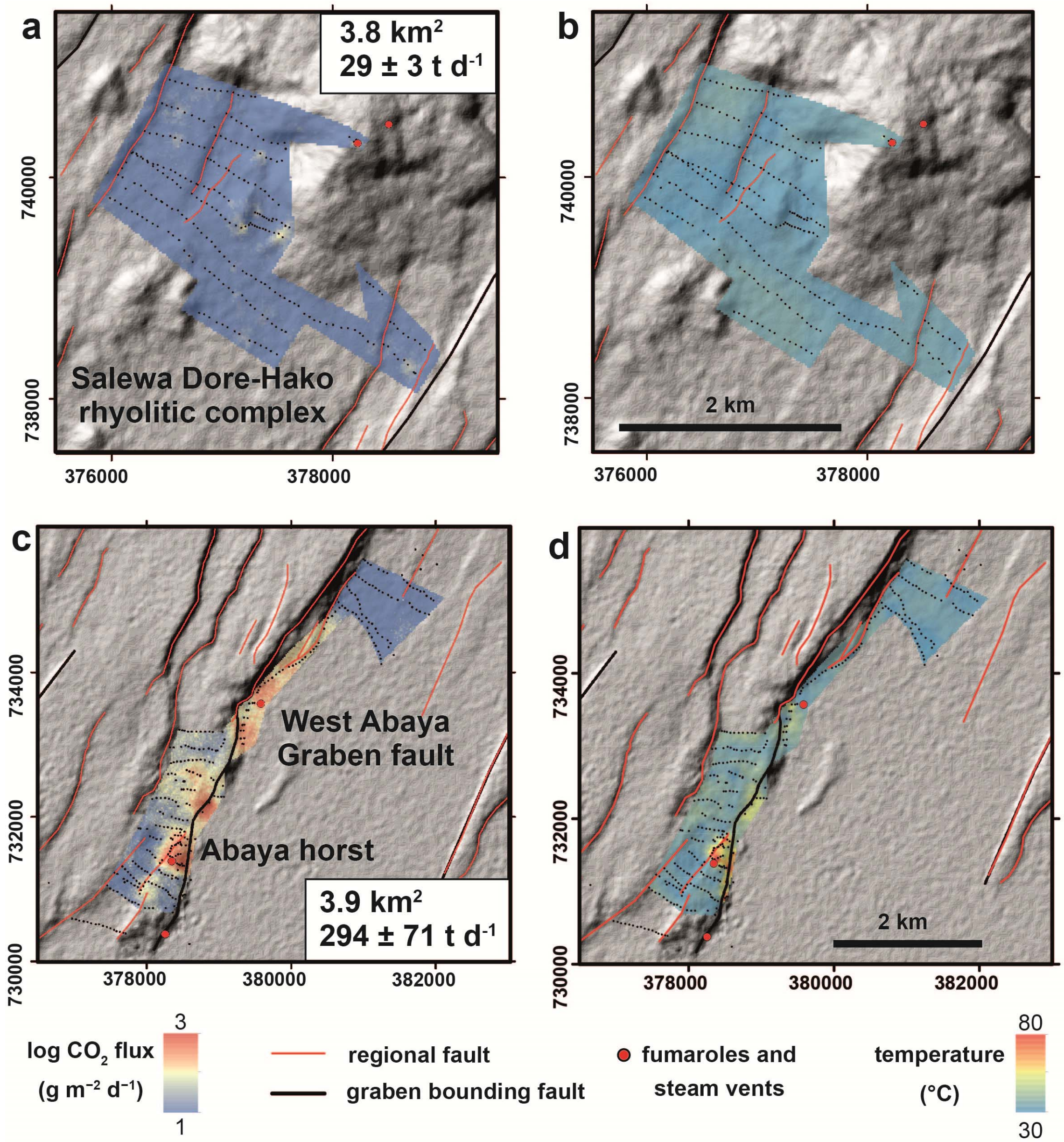

Figure 10. CO_2 flux and temperature maps derived using the sequential Gaussian simulation (sGs) approach for the Salewa Dore-Hako rhyolitic complex **(a, b)** and the West Abaya graben fault **(c, d)**. Black points represent a discrete flux measurement.

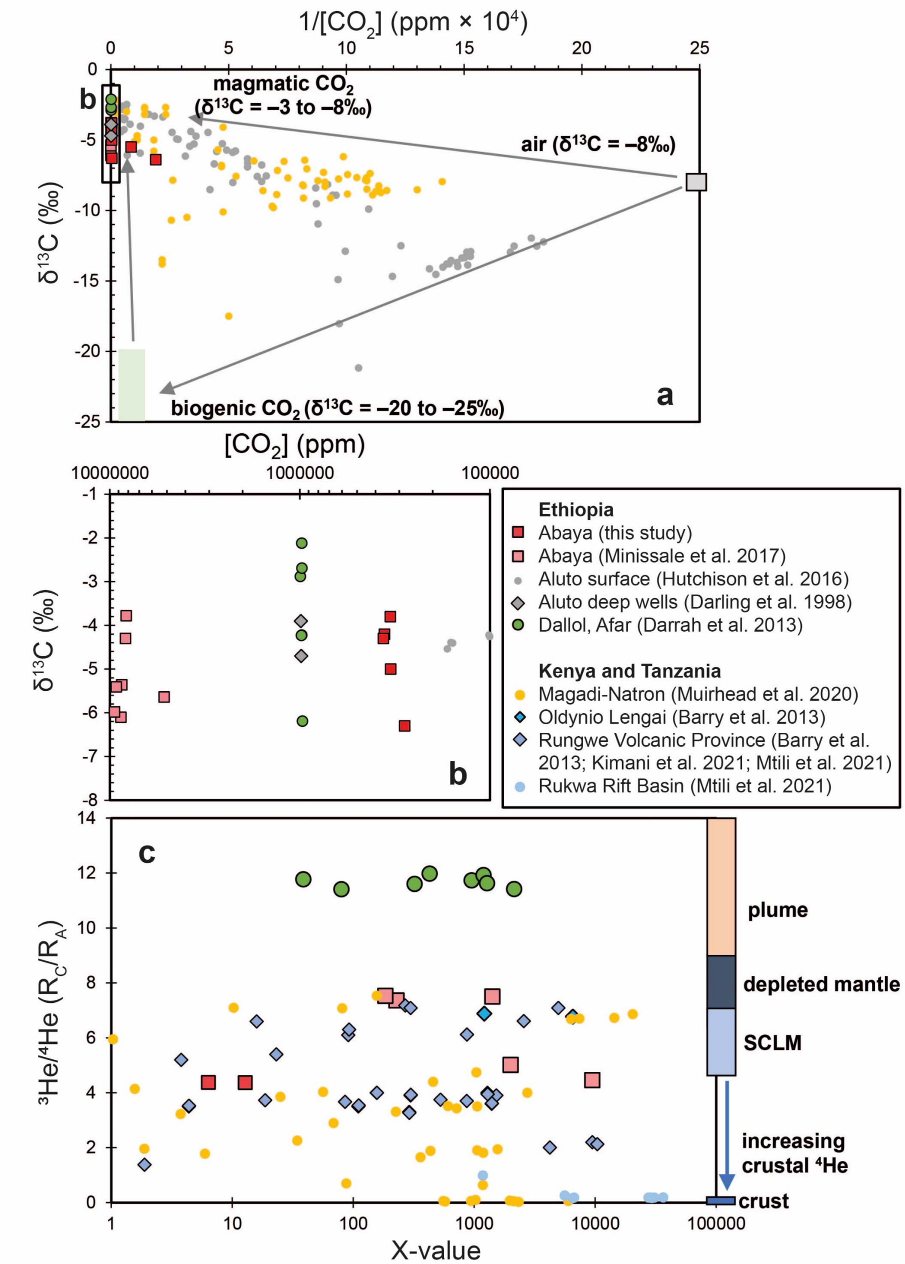

Figure 11. (a) Carbon isotopes ($\delta^{13}C$) of soil gas and fumarole samples from Ethiopian, Kenyan and Tanzania volcanic-hydrothermal systems. $\delta^{13}C$ of CO_2 is plotted against the reciprocal of CO_2 concentration in the sample. The data defines a triangular array defined by 3 endmembers: air, biogenic CO_2 (with characteristic light $\delta^{13}C$ of –20 and –25 ‰) and magmatic CO_2 (with $\delta^{13}C$ between –3 and –8 ‰). **(b)** Inset of Figure 11a showing $\delta^{13}C$ for the highest concentration samples (note the logarithmic rather than reciprocal scale). **(c)** He isotopes versus X-value. $^3He/^4He$ is corrected for air and given in R_C/R_A notation. The X-value is calculated as $(^4He/^{20}Ne)_{measured}$ / $(^4He/^{20}Ne)_{air}$ and provides an assessment of how much air has been entrained into the sample. X-values close to 1 are air-dominated, and those with much higher X-values indicate that very little air has been incorporated into the sample. Endmember $^3He/^4He$ for depleted mid-ocean ridge basalts (MORB), sub-continental lithospheric mantle (SLCM), plume and crust are shown on the left of the plot after values

from Gilfillan and Ballentine (2018), Bräuer et al. (2016), Hilton et al. (2011), Graham (2002) and Gautheron and Moreira (2002).

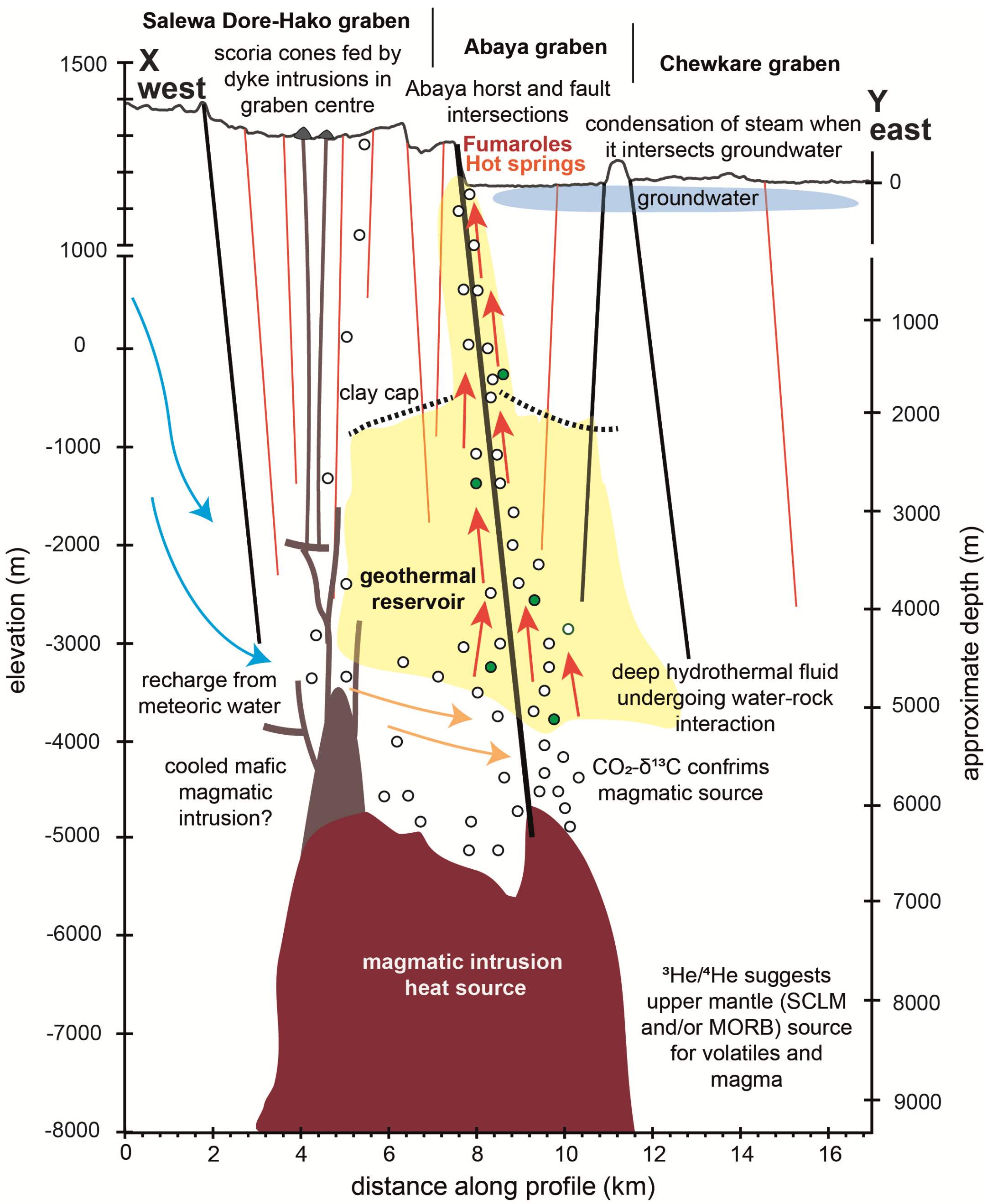

Figure 12. Schematic west-east cross section of the North Abaya geothermal system. The line of section correpsonds to the profile X-Y shown in Figure 2. Arrows show directions of fluid flow and their colour gives a qualititve indication of temperature. Deep magmatic intrusions are shown as red shaded area. Gases are represented by circles: white circles indicate magmatic volatiles, green circles indicate crustal ^4He addition. The West Abaya graben fault is the key fault structure in the region and directs the flow of magmatic volatiles and hydrothermal fluids to the surface.

Sample ID	Location	Temperature (°C)	Easting (m)	Northing (m)	CO_2	He	H_2	Ar	O_2	N_2	CH_4	CO	$\delta^{13}C$ (‰)	R/R_A	X-Value	R_C/R_A
AB-19-G01	SDHRC	50	378192	740329	1.2	0.00	1.0	0.7	17.6	79.3	0.0	0.2	-5.5			
AB-19-G03	WAGF (Abaya horst east)	97	378572	731024	31.7	0.00	0.0	1.1	21.6	44.6	0.5	0.4				
AB-19-G04	WAGF (Abaya horst east)	97	378572	731024	30.7	0.00	0.0	1.2	21.7	45.5	0.5	0.4				
AB-19-G08	WAGF (Abaya horst east)	94.5	378524	731134	0.4	0.00	0.0	1.1	31.4	66.3	0.1	0.6				
AB-19-PB-02	WAGF (Abaya horst east)	94.5	378524	731134	35.5	0.00	0.0	1.1	21.1	41.4	0.5	0.4		3.8	6	4.4
AB-18-G01	WAGF (Abaya horst west)	94	378353	731590	32.0	0.01	2.0	0.6	20.4	44.1	0.5	0.5				
AB-18-G02	WAGF (Abaya horst west)	94	378353	731590	33.2	0.15	3.4	0.6	19.2	42.4	0.5	0.4	-5.0			
AB-18-G03	WAGF (Abaya horst west)	94	378353	731590	33.4	0.01	1.9	0.6	19.4	43.8	0.5	0.4	-3.8			
AB-19-G02	WAGF (Abaya horst west)	97	378387	731603	5.3	0.00	0.0	1.1	20.7	72.7	0.1	0.2				
AB-19-G05	WAGF (Abaya horst west)	95	378337	731548	35.9	0.01	1.8	0.6	18.3	42.5	0.5	0.4	-4.2			
AB-19-G06	WAGF (Abaya horst west)	100	378354	731586	18.0	0.00	2.0	0.6	17.4	61.5	0.2	0.2				
AB-19-G07	WAGF (Abaya horst west)	94	378462	731729	36.3	0.00	1.7	0.6	19.1	40.9	0.6	0.8	-4.3			
AB-19-PB-03	WAGF (Abaya horst west)	93.5	378337	731548	35.7	0.00	0.0	1.1	19.6	43.1	0.1	0.4		4.1	13	4.4
AB-18-G04	WAGF (north of Abaya horst)	58	379479	733655	0.5	0.00	0.4	0.8	21.9	75.6	0.3	0.5	-6.4			
AB-18-G05	WAGF (north of Abaya horst)	58	379479	733655	28.1	0.00	2.7	0.6	14.7	53.8	0.1	0.1	-6.3			

Table 1. Composition of samples from North Abaya geothermal area. Samples were mainly collected from the West Abaya graben fault (WAGF). Although one sample is from the Salewa Dore-Hako rhyolitic complex (SDHRC). Gas concentrations are reported in mol %. Bulk gas chemistry and C isotopes were measured on samples collected in evacuated glass vials. He isotopes were measured on samples collected in Cu tubes. R/R_A is the measured $^3He/^4He$ divided by the $^3He/^4He$ in air. X-value is the $^4He/^{20}Ne$ ratio of the sample relative to that measured in air. R_C/R_A is the air corrected $^3He/^4He$ for the samples using the X-values (c.f. Hilton, 1996).

Study Area	CO_2 flux (t d^{-1})	Area (km^2)	CO_2 flux density (t km^{-2} d^{-1})	Reference
East African Rift				
Abaya volcanic field, Ethiopia (Western Abaya graben boundary fault)	294	3.9	75	This study
Aluto, Ethiopia (Artu Jawe fault zone)	57	0.8	71	Hutchison et al. (2015)
Oldoinyo Lengai, Tanzania *	100	3.14	32	Koepenick et al. (1996)
Magadi-Natron Basin, Kenya and Tanzania	11095	960	11	Lee et al. (2016)
Longonot volcano, Kenya	0.258	0.086	3	Robertson et al. (2016)
Comparable geothermal fields				
Rotorua geothermal system, Taupo Volcanic Zone, New Zealand	620	8.9	70	Werner and Cardellini (2006)
Reykjanes geothermal area, Iceland	13.5	0.22	61	Fridriksson et al. (2006)
Yanbajain geothermal area, China	138	3.2	43	Chiodini et al. (1998)
Cordón de Inacaliri Volcanic Complex, Chile	0.53	0.0179	30	Marco et al. (2021)
Hengill Volcano, Iceland	1526	168.1	9	Hernández et al. (2012)
Other volcanic systems				
Cerro Negro volcano, Nicaragua	2800	0.58	4828	Salazar et al. (2001)
Solfatara volcano, Italy	1500	1	1500	Chiodini et al. (2001)
El Chichón, Mexico (crater and crater lake)	370	0.308	1200	Mazot et al. (2011)
Nea Kameni, Santorini, Greece (summit area) †	21-38	0.02	1050-1900	Parks et al. (2013)
Mammoth Mountain, Horseshoe Lake (flank area)	104.3	0.13	802	Cardellini et al. (2003)
Teide volano, Spain (summit area)	380	0.53	717	Hernández et al. (1998)
Liu-Huang-Ku hydrothermal area, Taiwan (phreatic crater)	22.4	0.03	659	Lan et al. (2007)
Mud volcano, Yellowstone	1730	3.5	494	Werner et al. (2000)
Hot Spring Basin, Yellowstone	60	0.16	387	Werner et al. (2008)
Methana volcanic system, Greece	2.59	0.01	259	D'Alessandro et al. (2008)
Hakkoda volcanic area, Japan (localized flank area)	127	0.58	219	Hernández Perez et al. (2003)
Furnas volcano, São Miguel Island, Azores	968	5.2	186	Viveiros et al. (2003)
Miyakejima volcano, Japan (summit)	100-150	0.6	167	Hernández et al. (2001)
Planchón–Peteroa Volcanic Complex, Argentina and Chile	6.49	0.077	84	Lamberti et al. (2021)
Nisyros caldera, Greece	84	2	42	Cardellini et al. (2003)
Vulcano island, Italy (Western and Southern Slopes)	75	1.9	39	Chiodini et al. (1998)
Mount Epomeo, Italy (Western Flank)	32.6	0.86	38	Chiodini et al. (2004)
Iwojima volcano, Japan	760	22	35	Notsu et al. (2005)
Vesuvius, Italy	193.8	5.5	35	Frondini et al. (2004)
Cuicocha Caldera Lake, Ecuador	135	3.95	32	Sierra et al. (2021)
Satsuma-Iwojma volcano, Japan	80	2.5	32	Shimoike et al. (2002)
Pantelleria island, Italy	989	84	12	Favara et al. (2001)
Pululahua caldera, Ecuador	270	27.6	10	Padrón et al. (2008)

*Measurements assume CO_2 emission restricted to the summit and flank area with diameter of 2 km

†Measurements made across a period of volcanic unrest (Parks et al., 2013)

Table 2: Comparison of CO_2 flux for different volcanic and geothermal areas ordered by CO_2 flux density (t km^{-2} d^{-1}).

References

Acocella, V., Korme, T., Salvini, F., & Funiciello, R. (2003). Elliptic calderas in the Ethiopian Rift: Control of pre-existing structures. Journal of Volcanology and Geothermal Research, 119(1–4), 189–203. https://doi.org/10.1016/S0377-0273(02)00342-6

Agostini, A., Bonini, M., Corti, G., Sani, F., & Mazzarini, F. (2011). Fault architecture in the Main Ethiopian Rift and comparison with experimental models: Implications for rift evolution and Nubia-Somalia kinematics. Earth and Planetary Science Letters, 301(3–4), 479–492. https://doi.org/10.1016/j.epsl.2010.11.024

Agusto, M., Tassi, F., Caselli, A. T., Vaselli, O., Rouwet, D., Capaccioni, B., et al. (2013). Gas geochemistry of the magmatic-hydrothermal fluid reservoir in the Copahue-Caviahue Volcanic Complex (Argentina). Journal of Volcanology and Geothermal Research, 257, 44–56. https://doi.org/10.1016/j.jvolgeores.2013.03.003

Albino, F., & Biggs, J. (2021). Magmatic Processes in the East African Rift System: Insights From a 2015–2020 Sentinel-1 InSAR Survey. Geochemistry, Geophysics, Geosystems, 22(3), 1–24. https://doi.org/10.1029/2020GC009488

Albino, F., Biggs, J., Lazecký, M., & Maghsoudi, Y. (2022). Routine Processing and Automatic Detection of Volcanic Ground Deformation Using Sentinel-1 InSAR Data: Insights from African Volcanoes. Remote Sensing, 14(22), 5703. https://doi.org/10.3390/rs14225703

Barry, P. H., Hilton, D. R., Fischer, T. P., de Moor, J. M., Mangasini, F., & Ramirez, C. (2013). Helium and carbon isotope systematics of cold "mazuku" CO2 vents and hydrothermal gases and fluids from Rungwe Volcanic Province, southern Tanzania. Chemical Geology, 339(July), 141–156. https://doi.org/10.1016/j.chemgeo.2012.07.003

Barry, P. H., Lawson, M., Meurer, W. P., Warr, O., Mabry, J. C., Byrne, D. J., & Ballentine, C. J. (2016). Noble gases solubility models of hydrocarbon charge mechanism in the Sleipner Vest gas field. Geochimica et Cosmochimica Acta, 194, 291–309. https://doi.org/https://doi.org/10.1016/j.gca.2016.08.021

Bastow, I. D., Pilidou, S., Kendall, J., & Stuart, G. W. (2010). Melt-induced seismic anisotropy and magma assisted rifting in Ethiopia: Evidence from surface waves. Geochemistry, Geophysics, Geosystems, 11(6).

Bense, V. F., Gleeson, T., Loveless, S. E., Bour, O., & Scibek, J. (2013). Fault zone hydrogeology. Earth-Science Reviews, 127, 171–192. https://doi.org/10.1016/j.earscirev.2013.09.008

Biggs, J, Anthony, E. Y., & Ebinger, C. J. (2009). Multiple inflation and deflation events at Kenyan volcanoes, East African Rift. Geology, 37(11), 979–982. https://doi.org/10.1130/G30133A.1

Biggs, J, Bastow, I. D., Keir, D., & Lewi, E. (2011). Pulses of deformation reveal frequently recurring shallow magmatic activity beneath the Main Ethiopian Rift. Geochemistry, Geophysics, Geosystems, 12(9).

Biggs, Juliet, Ayele, A., Fischer, T. P., Fontijn, K., Hutchison, W., Kazimoto, E., et al. (2021). Volcanic activity and hazard in the East African Rift Zone. Nature Communications, 12(1), 1–12. https://doi.org/10.1038/s41467-021-27166-y

Birhanu, Y., Wilks, M., Biggs, J., Kendall, J., Ayele, A., & Lewi, E. (2018). Seasonal patterns of seismicity and deformation at the Alutu geothermal reservoir , Ethiopia , induced by hydrological loading. Journal of Volcanology and Geothermal Research, 356, 175–182. https://doi.org/10.1016/j.jvolgeores.2018.03.008

Boccaletti, M., Mazzuoli, R., Bonini, M., Trua, T., & Abebe, B. (1999). Plio-Quaternary volcanotectonic activity in the northern sector of the Main Ethiopian Rift: Relationships with oblique rifting. Journal of African Earth Sciences, 29(4), 679–698. https://doi.org/10.1016/S0899-5362(99)00124-4

Braddock, M., Biggs, J., Watson, I. M., Hutchison, W., Pyle, D. M., & Mather, T. A. (2017). Satellite observations of fumarole activity at Aluto volcano, Ethiopia: Implications for geothermal monitoring and volcanic hazard. Journal of Volcanology and Geothermal Research, 341. https://doi.org/10.1016/j.jvolgeores.2017.05.006

Bräuer, K., Geissler, W. H., Kämpf, H., Niedermannn, S., & Rman, N. (2016). Helium and carbon isotope signatures of gas exhalations in the westernmost part of the Pannonian Basin (SE Austria/NE Slovenia): Evidence for active lithospheric mantle degassing. Chemical Geology, 422, 60–70.

Burnside, N., Montcoudiol, N., Becker, K., & Lewi, E. (2021). Geothermal energy resources in Ethiopia: Status review and insights from hydrochemistry of surface and groundwaters. Wiley Interdisciplinary Reviews: Water, 8(6), 1–27. https://doi.org/10.1002/wat2.1554

Burton, M. R., Sawyer, G. M., & Granieri, D. (2013). Deep carbon emissions from volcanoes. Reviews in Mineralogy and Geochemistry, 75, 323–354. https://doi.org/10.2138/rmg.2013.75.11

Carapezza, M. L., & Granieri, D. (2004). CO2 soil flux at Vulcano (Italy): Comparison between active and passive methods. Applied Geochemistry, 19(1), 73–88. https://doi.org/10.1016/S0883-2927(03)00111-2

Cardellini, C., Chiodini, G., & Frondini, F. (2003). Application of stochastic simulation to CO 2 flux from soil: Mapping and quantification of gas release . Journal of Geophysical Research: Solid Earth, 108(B9). https://doi.org/10.1029/2002jb002165

Carn, S. A., Fioletov, V. E., Mclinden, C. A., Li, C., & Krotkov, N. A. (2017). A decade of global volcanic SO2 emissions measured from space. Scientific Reports, 7, 1–12. https://doi.org/10.1038/srep44095

Casey, M., Ebinger, C. J., Keir, D., Gloaguen, R., & Mohamed, F. (2006). Strain accommodation in transitional rifts: extension by magma intrusion and faulting in Ethiopian rift magmatic segments. Geological Society Special Publication, 259(2003), 143–163. https://doi.org/10.1144/GSL.SP.2006.259.01.13

Cheng, W. (1996). Measurement of rhizosphere respiration and organic matter decomposition using natural 13C. Plant and Soil, 183(2), 263–268.

Chernet, T. (2011). Geology and hydrothermal resources in the northern Lake Abaya area (Ethiopia). Journal of African Earth Sciences, 61(2), 129–141. https://doi.org/10.1016/j.jafrearsci.2011.05.006

Chiodini Frondini F., Cardellini C., Granieri D., Marini L., Ventura G., G. (2001). CO2 degassing and energy release at Solfatara volcano, Campi Flegrei, Italy. Journal of Geophysical Research, 106(B8), 9.

Chiodini, G., Cioni, R., Guidi, M., Raco, B., & Marini, L. (1998). Soil CO2 flux measurements in volcanic and geothermal areas. Applied Geochemistry, 13(5), 543–552. https://doi.org/10.1016/S0883-2927(97)00076-0

Chiodini, G., Caliro, S., Cardellini, C., Avino, R., Granieri, D., & Schmidt, A. (2008). Carbon isotopic composition of soil CO2 efflux, a powerful method to discriminate different sources feeding soil CO2 degassing in volcanic-hydrothermal areas. Earth and Planetary Science Letters, 274(3–4), 372–379. https://doi.org/10.1016/j.epsl.2008.07.051

Chiodini, Giovanni, Avino, R., Brombach, T., Caliro, S., Cardellini, C., De Vita, S., et al. (2004). Fumarolic and diffuse soil degassing west of Mount Epomeo, Ischia, Italy. Journal of Volcanology and Geothermal Research, 133(1–4), 291–309. https://doi.org/10.1016/S0377-0273(03)00403-7

Choi, J.-H., Edwards, P., Ko, K., & Kim, Y.-S. (2016). Definition and classification of fault damage zones: A review and a new methodological approach. Earth-Science Reviews, 152, 70–87.

Clarke, B., Tierz, P., Calder, E., & Yirgu, G. (2020). Probabilistic Volcanic Hazard Assessment for Pyroclastic Density Currents From Pumice Cone Eruptions at Aluto Volcano, Ethiopia. Frontiers in Earth Science, 8(August), 1–19. https://doi.org/10.3389/feart.2020.00348

Corti, G. (2009). Continental rift evolution: From rift initiation to incipient break-up in the Main Ethiopian Rift, East Africa. Earth-Science Reviews, 96(1–2), 1–53. https://doi.org/10.1016/j.earscirev.2009.06.005

Corti, G., Sani, F., Philippon, M., Sokoutis, D., Willingshofer, E., & Molin, P. (2013). Quaternary volcano-tectonic activity in the Soddo region, western margin of the Southern Main Ethiopian Rift. Tectonics, 32(4), 861–879. https://doi.org/10.1002/tect.20052

Corti, G., Molin, P., Sembroni, A., Bastow, I. D., & Keir, D. (2018). Control of Pre-rift Lithospheric Structure on the Architecture and Evolution of Continental Rifts: Insights From the Main Ethiopian Rift, East Africa. Tectonics, 37(2), 477–496. https://doi.org/10.1002/2017TC004799

Craig, H., Lupton, J. E., & Horowiff, R. M. (1977). Isotope geochemistry and hydrology of geothermal waters in the Ethiopian Rift Valley. UC San Diego: Scripps Institution of Oceanography.

Curewitz, D., & Karson, J. A. (1997). Structural settings of hydrothermal outflow: Fracture permeability maintained by fault propagation and interaction. Journal of Volcanology and Geothermal Research, 79(3–4), 149–168. https://doi.org/10.1016/S0377-0273(97)00027-9

D'Alessandro, W., Brusca, L., Kyriakopoulos, K., Michas, G., & Papadakis, G. (2008). Methana, the westernmost active volcanic system of the south Aegean arc (Greece): Insight from fluids geochemistry. Journal of Volcanology and Geothermal Research, 178(4), 818–828. https://doi.org/10.1016/j.jvolgeores.2008.09.014

Darling, W. G. (1998). Hydrothermal hydrocarbon gases: 2, application in the East African rift system. Applied Geochemistry, 13(7), 825–840. https://doi.org/10.1016/S0883-2927(98)00022-5

Darling, W. G., Griesshaber, E., Andrews, J. N., Armannsson, H., & O'Nions, R. K. (1995). The origin of hydrothermal and other gases in the Kenya Rift Valley. Geochimica et Cosmochimica Acta, 59(12), 2501–2512. https://doi.org/10.1016/0016-7037(95)00145-X

Darling, W. George, Gizaw, B., & Arusei, M. K. (1996). Lake-groundwater relationships and fluid-rock interaction in the East African Rift Valley: Isotopic evidence. Journal of African Earth Sciences, 22(4), 423–431. https://doi.org/10.1016/0899-5362(96)00026-7

Darrah, T. H., Tedesco, D., Tassi, F., Vaselli, O., Cuoco, E., & Poreda, R. J. (2013). Gas chemistry of the Dallol region of the Danakil Depression in the Afar region of the northern-most East African Rift. Chemical Geology, 339, 16–29. https://doi.org/10.1016/j.chemgeo.2012.10.036

Day, J. M. D., Barry, P. H., Hilton, D. R., Burgess, R., Pearson, D. G., & Taylor, L. A. (2015). The helium flux from the continents and ubiquity of low-3He/4He recycled crust and lithosphere. Geochimica et Cosmochimica Acta, 153, 116–133.

Deutsch, C. V., & Journel, A. G. (1998). GSLIB: Geostatistical Software Library and User's Guide (2nd ed.). New York: Oxford University Press. https://doi.org/10.1017/s0016756899531774

Ebinger, C. (2005). Continental break-up: The East African perspective. Astronomy and Geophysics, 46(2), 2.16-2.21. https://doi.org/10.1111/j.1468-4004.2005.46216.x

Ebinger, C. J., & Casey, M. (2001). Continental breakup in magmatic provinces: An Ethiopian example. Geology, 29(6), 527–530. https://doi.org/10.1130/0091-7613(2001)029<0527:CBIMPA>2.0.CO;2

Faulkner, D. R., Mitchell, T. M., Jensen, E., & Cembrano, J. (2011). Scaling of fault damage zones with displacement and the implications for fault growth processes. Journal of Geophysical Research: Solid Earth, 116(B5).

Favara, R., Giammanco, S., Inguaggiato, S., & Pecoraino, G. (2001). Preliminary estimate of CO2 output from Pantelleria Island volcano (Sicily, Italy): Evidence of active mantle degassing. Applied Geochemistry, 16(7–8), 883–894. https://doi.org/10.1016/S0883-2927(00)00055-X

Fischer, T. P., Arellano, S., Carn, S., Aiuppa, A., Galle, B., Allard, P., et al. (2019). The emissions of CO2 and other volatiles from the world's subaerial volcanoes. Scientific Reports, 9(1), 1–11. https://doi.org/10.1038/s41598-019-54682-1

Fontijn, K., McNamara, K., Zafu Tadesse, A., Pyle, D. M., Dessalegn, F., Hutchison, W., et al. (2018). Contrasting styles of post-caldera volcanism along the Main Ethiopian Rift: Implications for contemporary volcanic hazards. Journal of Volcanology and Geothermal Research. https://doi.org/10.1016/j.jvolgeores.2018.02.001

Fridriksson, T., Kristjánsson, B. R., Ármannsson, H., Margrétardóttir, E., Ólafsdóttir, S., & Chiodini, G. (2006). CO2 emissions and heat flow through soil, fumaroles, and steam heated mud pools at the Reykjanes geothermal area, SW Iceland. Applied Geochemistry, 21(9), 1551–1569. https://doi.org/10.1016/j.apgeochem.2006.04.006

Frondini, F., Chiodini, G., Caliro, S., Cardellini, C., Granieri, D., & Ventura, G. (2004). Diffuse CO2 degassing at Vesuvio, Italy. Bulletin of Volcanology, 66(7), 642–651. https://doi.org/10.1007/s00445-004-0346-x

Gautheron, C., & Moreira, M. (2002). Helium signature of the subcontinental lithospheric mantle. Earth and Planetary Science Letters, 199(1–2), 39–47.

Gerlach, T. M., & Taylor, B. E. (1990). Carbon isotope constraints on degassing of carbon dioxide from Kilauea Volcano. Geochimica et Cosmochimica Acta, 54(7), 2051–2058.

Giammanco, S., Parello, F., Gambardella, B., Schifano, R., Pizzullo, S., & Galante, G. (2007). Focused and diffuse effluxes of CO2 from mud volcanoes and mofettes south of Mt. Etna (Italy). Journal of Volcanology and Geothermal Research, 165(1–2), 46–63. https://doi.org/10.1016/j.jvolgeores.2007.04.010

Gianelli, G., & Teklemariam, M. (1993). Water-rock interaction processes in the Aluto-Langano geothermal field (Ethiopia). Journal of Volcanology and Geothermal Research, 56(4), 429–445. https://doi.org/10.1016/0377-0273(93)90007-E

Gibson, I. L. (1969). The structure and volcanic geology of an axial portion of the Main Ethiopian Rift. Tectonophysics, 8(4–6), 561–565. https://doi.org/10.1016/0040-1951(69)90054-7

Gilfillan, S. M. V., & Ballentine, C. J. (2018). He, Ne and Ar 'snapshot' of the subcontinental lithospheric mantle from CO2 well gases. Chemical Geology, 480(September 2017), 116–127. https://doi.org/10.1016/j.chemgeo.2017.09.028

Gleeson, M. L. M., Stock, M. J., Pyle, D. M., Mather, T. A., Hutchison, W., Yirgu, G., & Wade, J. (2017). Constraining magma storage conditions at a restless volcano in the Main Ethiopian Rift using phase equilibria models. Journal of Volcanology and Geothermal Research, 337. https://doi.org/10.1016/j.jvolgeores.2017.02.026

Graham, D. W. (2002). Noble gas isotope geochemistry of mid-ocean ridge and ocean island basalts: Characterization of mantle source reservoirs. Reviews in Mineralogy and Geochemistry, 47(1), 247–317. https://doi.org/10.2138/rmg.2002.47.8

Hernández, P., Notsu, K., Tsurumi, M., Mori, T., Ohno, M., Shimoike, Y., et al. (2003). Carbon dioxide emissions from soils at Hakkoda, north Japan. Journal of Geophysical Research: Solid Earth, 108(B4), 1–10. https://doi.org/10.1029/2002jb001847

Hernández, P. A. (1998). Diffuse emission of carbon dioxide, methand and helium-3 from Teide volcano, Tenerife, Canary Islands. Geophysical Research Letters, 25(17), 3311–3314.

Hernández, P. A., Salazar, J. M., Shimoike, Y., Mori, T., Notsu, K., & Pérez, N. (2001). Diffuse emission of CO2 from Miyakejima volcano, Japan. Chemical Geology, 177(1–2), 175–185. https://doi.org/10.1016/S0009-2541(00)00390-9

Hernández, P. A., Pérez, N. M., Fridriksson, T., Egbert, J., Ilyinskaya, E., Thárhallsson, A., et al. (2012). Diffuse volcanic degassing and thermal energy release from Hengill volcanic system, Iceland. Bulletin of Volcanology, 74(10), 2435–2448.

Hilton, D. R., Halldórsson, S. A., Barry, P. H., Fischer, T. P., De Moor, J. M., Ramirez, C. J., et al. (2011). Helium isotopes at Rungwe Volcanic Province, Tanzania, and the origin of East African Plateaux. Geophysical Research Letters, 38(21), 1–5. https://doi.org/10.1029/2011GL049589

Hilton, David R. (1996). The helium and carbon isotope systematics of a continental geothermal system: results from monitoring studies at Long Valley caldera (California, U.S.A.). Chemical Geology, 127(4), 269–295. https://doi.org/https://doi.org/10.1016/0009-2541(95)00134-4

Hochstein, M. P., Oluma, B., & Hole, H. (2017). Early exploration of the Aluto geothermal field, Ethiopia (History of discovery well LA-3). Geothermics, 66, 73–84. https://doi.org/10.1016/j.geothermics.2016.11.010

Hübert, J., Whaler, K., & Fisseha, S. (2018). The Electrical Structure of the Central Main Ethiopian Rift as Imaged by Magnetotellurics: Implications for Magma Storage and

Pathways. Journal of Geophysical Research: Solid Earth, 123(7), 6019–6032. https://doi.org/10.1029/2017JB015160

Hunt, J. A., Zafu, A., Mather, T. A., Pyle, D. M., & Barry, P. H. (2017). Spatially Variable CO2 Degassing in the Main Ethiopian Rift: Implications for Magma Storage, Volatile Transport, and Rift-Related Emissions. Geochemistry, Geophysics, Geosystems, 18(10), 3714–3737. https://doi.org/10.1002/2017GC006975

Hunt, J. A., Pyle, D. M., & Mather, T. A. (2019). The Geomorphology, Structure, and Lava Flow Dynamics of Peralkaline Rift Volcanoes From High-Resolution Digital Elevation Models. Geochemistry, Geophysics, Geosystems, 20(3), 1508–1538. https://doi.org/10.1029/2018GC008085

Hunt, J. A., Mather, T. A., & Pyle, D. M. (2020). Morphological comparison of distributed volcanic fields in the Main Ethiopian Rift using high-resolution digital elevation models. Journal of Volcanology and Geothermal Research, 393, 106732. https://doi.org/10.1016/j.jvolgeores.2019.106732

Hutchison, W., Mather, T. A., Pyle, D. M., Biggs, J., & Yirgu, G. (2015). Structural controls on fluid pathways in an active rift system: A case study of the Aluto volcanic complex. Geosphere, 11(3). https://doi.org/10.1130/GES01119.1

Hutchison, W., Biggs, J., Mather, T. A., Pyle, D. M., Lewi, E., Yirgu, G., et al. (2016). Causes of unrest at silicic calderas in the East African Rift: New constraints from InSAR and soil-gas chemistry at Aluto volcano, Ethiopia. Geochemistry, Geophysics, Geosystems, 17(8). https://doi.org/10.1002/2016GC006395

Hutchison, W., Mather, T. A., Pyle, D. M., Boyce, A. J., Gleeson, M. L. M., Yirgu, G., et al. (2018). The evolution of magma during continental rifting: New constraints from the isotopic and trace element signatures of silicic magmas from Ethiopian volcanoes. Earth and Planetary Science Letters, 489. https://doi.org/10.1016/j.epsl.2018.02.027

Iddon, F., & Edmonds, M. (2020). Volatile-Rich Magmas Distributed Through the Upper Crust in the Main Ethiopian Rift. Geochemistry, Geophysics, Geosystems, 21(6). https://doi.org/10.1029/2019GC008904

Iddon, F., Jackson, C., Hutchison, W., Fontijn, K., Pyle, D. M., Mather, T. A., et al. (2019). Mixing and Crystal Scavenging in the Main Ethiopian Rift Revealed by Trace Element

Systematics in Feldspars and Glasses. Geochemistry, Geophysics, Geosystems, 20(1), 230–259. https://doi.org/10.1029/2018GC007836

Javoy, M., & Pineau, F. (1991). The volatiles record of a “popping” rock from the Mid-Atlantic Ridge at 14 N: chemical and isotopic composition of gas trapped in the vesicles. Earth and Planetary Science Letters, 107(3–4), 598–611.

Jolie, E., Hutchison, W., Driba, D. L., Jentsch, A., & Gizaw, B. (2019). Pinpointing Deep Geothermal Upflow in Zones of Complex Tectono-Volcanic Degassing: New Insights from Aluto Volcano, Main Ethiopian Rift. Geochemistry, Geophysics, Geosystems, 20(8), 4146–4161. https://doi.org/10.1029/2019GC008309

Keir, D., Ebinger, C. J., Stuart, G. W., Daly, E., & Ayele, A. (2006). Strain accommodation by magmatism and faulting as rifting proceeds to breakup: Seismicity of the northern Ethiopian rift. Journal of Geophysical Research: Solid Earth, 111(5), 1–17. https://doi.org/10.1029/2005JB003748

Kendall, J. M., Stuart, G. W., Ebinger, C. J., Bastow, I. D., & Keir, D. (2005). Magma-assisted rifting in Ethiopia. Nature, 433(7022), 146–148. https://doi.org/10.1038/nature03161

Kennedy, B. M., Lynch, M. A., Reynolds, J. H., & Smith, S. P. (1985). Intensive sampling of noble gases in fluids at Yellowstone: I. Early overview of the data; regional patterns. Geochimica et Cosmochimica Acta, 49(5), 1251–1261. https://doi.org/https://doi.org/10.1016/0016-7037(85)90014-6

Kimani, C. N., Kasanzu, C. H., Tyne, R. L., Mtili, K. M., Byrne, D. J., Kazimoto, E. O., et al. (2021). He, Ne, Ar and CO2 systematics of the Rungwe Volcanic Province, Tanzania: Implications for fluid source and dynamics. Chemical Geology, 586(July), 120584. https://doi.org/10.1016/j.chemgeo.2021.120584

Knott, S. D., Beach, A., Brockbank, P. J., Brown, J. L., McCallum, J. E., & Welbon, A. I. (1996). Spatial and mechanical controls on normal fault populations. Journal of Structural Geology, 18(2–3), 359–372.

Koepenick, K. W., Brantley, S. L., Thompson, J. M., Rowe, G. L., Nyblade, A. A., & Moshy, C. (1996). Volatile emissions from the crater and flank of Oldoinyo Lengai volcano, Tanzania. Journal of Geophysical Research: Solid Earth, 101(6), 13819–13830. https://doi.org/10.1029/96jb00173

Kogan, L., Fisseha, S., Bendick, R., Reilinger, R., McClusky, S., King, R., & Solomon, T. (2012). Lithospheric strength and strain localization in continental extension from observations of the East African Rift. Journal of Geophysical Research: Solid Earth, 117(3), 1–16. https://doi.org/10.1029/2011JB008516

Kombe, E. Y., & Muguthu, J. (2018). Geothermal Energy Development in East Africa: Barriers and Strategies. Journal of Energy Research and Reviews, (December 2018), 1–6. https://doi.org/10.9734/jenrr/2019/v2i129722

Lamberti, M. C., Agusto, M., Llano, J., Nogués, V., Venturi, S., Vélez, M. L., et al. (2021). Soil CO2 flux baseline in Planchón–Peteroa Volcanic Complex, Southern Andes, Argentina-Chile. Journal of South American Earth Sciences, 105, 102930.

Lan, T. F., Yang, T. F., Lee, H. F., Chen, Y. G., Chen, C. H., Song, S. R., & Tsao, S. (2007). Compositions and flux of soil gas in Liu-Huang-Ku hydrothermal area, northern Taiwan. Journal of Volcanology and Geothermal Research, 165(1–2), 32–45. https://doi.org/10.1016/j.jvolgeores.2007.04.015

Lee, H., Muirhead, J. D., Fischer, T. P., Ebinger, C. J., Kattenhorn, S. A., Sharp, Z. D., & Kianji, G. (2016). Massive and prolonged deep carbon emissions associated with continental rifting. Nature Geoscience, 9(2), 145–149. https://doi.org/10.1038/ngeo2622

Lee, H., Fischer, T. P., Muirhead, J. D., Ebinger, C. J., Kattenhorn, S. A., Sharp, Z. D., et al. (2017). Incipient rifting accompanied by the release of subcontinental lithospheric mantle volatiles in the Magadi and Natron basin, East Africa. Journal of Volcanology and Geothermal Research, 346, 118–133. https://doi.org/10.1016/j.jvolgeores.2017.03.017

Lloyd, R., Biggs, J., Wilks, M., Nowacki, A., Kendall, J. M., Ayele, A., et al. (2018). Evidence for cross rift structural controls on deformation and seismicity at a continental rift caldera. Earth and Planetary Science Letters, 487, 190–200. https://doi.org/10.1016/j.epsl.2018.01.037

Lloyd, R., Biggs, J., Birhanu, Y., Wilks, M., Gottsmann, J., Kendall, J. M., et al. (2018). Sustained Uplift at a Continental Rift Caldera. Journal of Geophysical Research: Solid Earth, 123(6), 5209–5226. https://doi.org/10.1029/2018JB015711

Macpherson, C., & Mattey, D. (1994). Carbon isotope variations of CO2 in Central Lau Basin basalts and ferrobasalts. Earth and Planetary Science Letters, 121(3–4), 263–276.

Marco, T., Barbara, N., Orlando, V., Santiago, M., Diego, M., & Alberto, R. (2021). Geothermics ´ n de Soil CO 2 flux and temperature from a new geothermal area in the Cord o Inacaliri Volcanic Complex (northern Chile). Geothermics, 89(June 2020), 101961. https://doi.org/10.1016/j.geothermics.2020.101961

Mazot, A., Rouwet, D., Taran, Y., Inguaggiato, S., & Varley, N. (2011). CO_2 and He degassing at El Chichón volcano, Chiapas, Mexico: Gas flux, origin and relationship with local and regional tectonics. Bulletin of Volcanology, 73(4), 423–441. https://doi.org/10.1007/s00445-010-0443-y

Mazzarini, F., Rooney, T. O., & Isola, I. (2013). The intimate relationship between strain and magmatism: A numerical treatment of clustered monogenetic fields in the Main Ethiopian Rift. Tectonics, 32(1), 49–64.

Mielnick, P. C., & Dugas, W. A. (2000). Soil CO_2 flux in a tallgrass prairie. Soil Biology and Biochemistry, 32(2), 221–228. https://doi.org/10.1016/S0038-0717(99)00150-9

Minissale, A., Corti, G., Tassi, F., Darrah, T. H., Vaselli, O., Montanari, D., et al. (2017). Geothermal potential and origin of natural thermal fluids in the northern Lake Abaya area, Main Ethiopian Rift, East Africa. Journal of Volcanology and Geothermal Research, 336, 1–18. https://doi.org/10.1016/j.jvolgeores.2017.01.012

Mohr, P. A. (1967). Major volcano–tectonic lineament in the Ethiopian rift system. Nature, 213(5077), 664–665.

Molin, P., & Corti, G. (2015). Topography, river network and recent fault activity at the margins of the Central Main Ethiopian Rift (East Africa). Tectonophysics, 664, 67–82. https://doi.org/10.1016/j.tecto.2015.08.045

Mtili, K. M., Byrne, D. J., Tyne, R. L., Kazimoto, E. O., Kimani, C. N., Kasanzu, C. H., et al. (2021). The origin of high helium concentrations in the gas fields of southwestern Tanzania. Chemical Geology, 585(July), 120542. https://doi.org/10.1016/j.chemgeo.2021.120542

Muirhead, J. D., Kattenhorn, S. A., Lee, H., Mana, S., Turrin, B. D., Fischer, T. P., et al. (2016). Evolution of upper crustal faulting assisted by magmatic volatile release during early-stage continental rift development in the East African Rift. Geosphere, 12(6), 1670–1700. https://doi.org/10.1130/GES01375.1

Muirhead, James D., Fischer, T. P., Oliva, S. J., Laizer, A., van Wijk, J., Currie, C. A., et al. (2020). Displaced cratonic mantle concentrates deep carbon during continental rifting. Nature, 582(7810), 67–72. https://doi.org/10.1038/s41586-020-2328-3

Mulibo, G. D., & Nyblade, A. A. (2013). The P and S wave velocity structure of the mantle beneath eastern Africa and the African superplume anomaly. Geochemistry, Geophysics, Geosystems, 14(8), 2696–2715.

Notsu, K., Sugiyama, K., Hosoe, M., Uemura, A., Shimoike, Y., Tsunomori, F., et al. (2005). Diffuse CO2 efflux from Iwojima volcano, Izu-Ogasawara arc, Japan. Journal of Volcanology and Geothermal Research, 139(3–4), 147–161. https://doi.org/10.1016/j.jvolgeores.2004.08.003

Nowacki, A., Wilks, M., Kendall, J. M., Biggs, J., & Ayele, A. (2018). Characterising hydrothermal fluid pathways beneath Aluto volcano, Main Ethiopian Rift, using shear wave splitting. Journal of Volcanology and Geothermal Research, 356, 331–341. https://doi.org/10.1016/j.jvolgeores.2018.03.023

Ogden, C. S., Keir, D., Bastow, I. D., Ayele, A., Marcou, S., Ugo, F., et al. (2021). Seismicity and Crustal Structure of the Southern Main Ethiopian Rift: New Evidence From Lake Abaya. Geochemistry, Geophysics, Geosystems, 22(8), 1–17. https://doi.org/10.1029/2021GC009831

Omenda, P. A. (1998). The geology and structural controls of the Olkaria geothermal system, Kenya. Geothermics, 27(1), 55–74. https://doi.org/10.1016/S0375-6505(97)00028-X

Padrón, E., Hernández, P. A., Toulkeridis, T., Pérez, N. M., Marrero, R., Melián, G., et al. (2008). Diffuse CO2 emission rate from Pululahua and the lake-filled Cuicocha calderas, Ecuador. Journal of Volcanology and Geothermal Research, 176(1), 163–169. https://doi.org/10.1016/j.jvolgeores.2007.11.023

Pantaleo, M., & Walter, T. R. (2014). The ring-shaped thermal field of Stefanos crater, Nisyros Island: A conceptual model. Solid Earth, 5(1), 183–198. https://doi.org/10.5194/se-5-183-2014

Parkinson, K. J. (1981). An Improved Method for Measuring Soil Respiration in the Field. The Journal of Applied Ecology, 18(1), 221. https://doi.org/10.2307/2402491

Parks, M. M., Caliro, S., Chiodini, G., Pyle, D. M., Mather, T. A., Berlo, K., et al. (2013). Distinguishing contributions to diffuse CO2 emissions in volcanic areas from magmatic degassing and thermal decarbonation using soil gas 222Rn-δ13C systematics: Application to Santorini volcano, Greece. Earth and Planetary Science Letters, 377–378, 180–190. https://doi.org/10.1016/j.epsl.2013.06.046

Peccerillo, A., Barberio, M. R., Yirgu, G., Ayalew, D., Barbieri, M., & Wu, T. W. (2003). Relationships between mafic and peralkaline silicic magmatism in continental rift settings: A petrological, geochemical and isotopic study of the Gedemsa volcano, Central Ethiopian rift. Journal of Petrology, 44(11), 2003–2032. https://doi.org/10.1093/petrology/egg068

Person, M., Hofstra, A., Sweetkind, D., Stone, W., Cohen, D., Gable, C. W., & Banerjee, A. (2012). Analytical and numerical models of hydrothermal fluid flow at fault intersections. Geofluids, 12(4), 312–326.

Pizzi, A., Coltorti, M., Abebe, B., Disperati, L., Sacchi, G., & Salvini, R. (2006). The Wonji fault belt (Main Ethiopian Rift): Structural and geomorphological constraints and GPS monitoring. Geological Society Special Publication, 259, 191–207. https://doi.org/10.1144/GSL.SP.2006.259.01.16

Pürschel, M., Gloaguen, R., & Stadler, S. (2013). Geothermal activities in the Main Ethiopian Rift: Hydrogeochemical characterization of geothermal waters and geothermometry applications (Dofan-Fantale, Gergede-Sodere, Aluto-Langano). Geothermics, 47, 1–12. https://doi.org/10.1016/j.geothermics.2013.01.001

Rango, T., Petrini, R., Stenni, B., Bianchini, G., Slejko, F., Beccaluva, L., & Ayenew, T. (2010). The dynamics of central Main Ethiopian Rift waters: Evidence from δD, δ18O and 87Sr/86Sr ratios. Applied Geochemistry, 25(12), 1860–1871. https://doi.org/https://doi.org/10.1016/j.apgeochem.2010.10.001

Remy, N., Boucher, A., & Wu, J. (2009). Applied geostatistics with SGeMS: A user's guide. Cambridge University Press.

Rey, A., Pegoraro, E., Tedeschi, V., De Parri, I., Jarvis, P. G., & Valentini, R. (2002). Annual variation in soil respiration and its components in a coppice oak forest in Central Italy. Global Change Biology, 8(9), 851–866. https://doi.org/10.1046/j.1365-2486.2002.00521.x

Ritsema, J., Heijst, H. J. van, & Woodhouse, J. H. (1999). Complex shear wave velocity structure imaged beneath Africa and Iceland. Science, 286(5446), 1925–1928.

Ritsema, J., Deuss, A., Van Heijst, H. J., & Woodhouse, J. H. (2011). S40RTS: a degree-40 shear-velocity model for the mantle from new Rayleigh wave dispersion, teleseismic traveltime and normal-mode splitting function measurements. Geophysical Journal International, 184(3), 1223–1236.

Robertson, E., Biggs, J., Edmonds, M., Clor, L., Fischer, T. P., Vye-Brown, C., et al. (2016). Diffuse degassing at Longonot volcano, Kenya: Implications for CO2 flux in continental rifts. Journal of Volcanology and Geothermal Research, 327, 208–222. https://doi.org/10.1016/j.jvolgeores.2016.06.016

Robertson, E. A. M., Biggs, J., Cashman, K. V., Floyd, M. A., & Vye-Brown, C. (2016). Influence of regional tectonics and pre-existing structures on the formation of elliptical calderas in the Kenyan Rift. Geological Society Special Publication, 420(1), 43–67. https://doi.org/10.1144/SP420.12

Rooney, T. O., Bastow, I. D., & Keir, D. (2011). Insights into extensional processes during magma assisted rifting : Evidence from aligned scoria cones. Journal of Volcanology and Geothermal Research, 201(1–4), 83–96. https://doi.org/10.1016/j.jvolgeores.2010.07.019

Rooney, T. O., Hart, W. K., Hall, C. M., Ayalew, D., Ghiorso, M. S., Hidalgo, P., & Yirgu, G. (2012). Peralkaline magma evolution and the tephra record in the Ethiopian Rift. Contributions to Mineralogy and Petrology, 164(3), 407–426. https://doi.org/10.1007/s00410-012-0744-6

Rooney, T. O., Hanan, B. B., Graham, D. W., Furman, T., Blichert-toft, J., & Schilling, J. G. (2012). Upper mantle pollution during Afar plume-continental rift interaction. Journal of Petrology, 53(2), 365–389. https://doi.org/10.1093/petrology/egr065

Salazar, J. M. L., Hernández, P. A., Pérez, N. M., Melián, G., Álvarez, J., Segura, F., & Notsu, K. (2001). Diffuse emission of carbon dioxide from Cerro Negro volcano, Nicaragua, Central America. Geophysical Research Letters, 28(22), 4275–4278. https://doi.org/10.1029/2001GL013709

Samrock, F., Kuvshinov, A., Bakker, J., Jackson, A., & Fisseha, S. (2015). 3-D analysis and interpretation of magnetotelluric data from the Aluto-Langano geothermal field, Ethiopia. Geophysical Journal International, 202(3), 1923–1948. https://doi.org/10.1093/gji/ggv270

Samrock, Friedemann, Grayver, A. V., Eysteinsson, H., & Saar, M. O. (2018). Magnetotelluric Image of Transcrustal Magmatic System Beneath the Tulu Moye Geothermal Prospect in the Ethiopian Rift. Geophysical Research Letters, 45(23), 12,847-12,855. https://doi.org/10.1029/2018GL080333

Sano, Y., & Marty, B. (1995). Origin of carbon in fumarolic gas from island arcs. Chemical Geology, 119(1–4), 265–274.

Saria, E., Calais, E., Stamps, D. S., Delvaux, D., & Hartnady, C. J. H. (2014). Present-day kinematics of the East African Rift. Journal of Geophysical Research: Solid Earth, 119(4), 3584–3600. https://doi.org/10.1002/2013JB010901

Schöpa, A., Pantaleo, M., & Walter, T. R. (2011). Scale-dependent location of hydrothermal vents: Stress field models and infrared field observations on the Fossa Cone, Vulcano Island, Italy. Journal of Volcanology and Geothermal Research, 203(3–4), 133–145. https://doi.org/10.1016/j.jvolgeores.2011.03.008

Shimoike, Y., Kazahaya, K., & Shinohara, H. (2002). Soil gas emission of volcanic CO2 at Satsuma-Iwojima volcano, Japan. Earth, Planets and Space, 54(3), 239–247. https://doi.org/10.1186/BF03353023

Sierra, D., Hidalgo, S., Almeida, M., Vigide, N., Lamberti, M. C., Proaño, A., & Narváez, D. F. (2021). Temporal and spatial variations of CO2 diffuse volcanic degassing on Cuicocha Caldera Lake–Ecuador. Journal of Volcanology and Geothermal Research, 411, 107145.

Simiyu, S. M., & Keller, G. R. (2000). Seismic monitoring of the Olkaria Geothermal area, Kenya Rift valley. Journal of Volcanology and Geothermal Research, 95(1–4), 197–208. https://doi.org/10.1016/S0377-0273(99)00124-9

Sperrevik, S., Gillespie, P. A., Fisher, Q. J., Halvorsen, T., & Knipe, R. J. (2002). Empirical estimation of fault rock properties. In Norwegian Petroleum Society Special Publications (Vol. 11, pp. 109–125). Elsevier.

Tassi, F., Vaselli, O., Papazachos, C. B., Giannini, L., Chiodini, G., Vougioukalakis, G. E., et al. (2013). Geochemical and isotopic changes in the fumarolic and submerged gas discharges during the 2011-2012 unrest at Santorini caldera (Greece). Bulletin of Volcanology, 75(4), 1–15. https://doi.org/10.1007/s00445-013-0711-8

Tedesco, D., Tassi, F., Vaselli, O., Poreda, R. J., Darrah, T., Cuoco, E., & Yalire, M. M. (2010). Gas isotopic signatures (He, C, and Ar) in the Lake Kivu region (western branch of the East African rift system): Geodynamic and volcanological implications. Journal of Geophysical Research: Solid Earth, 115(1), 1–12. https://doi.org/10.1029/2008JB006227

Temtime, T., Biggs, J., Lewi, E., Hamling, I., Wright, T., & Ayele, A. (2018). Spatial and temporal patterns of deformation at the Tendaho geothermal prospect, Ethiopia. Journal of

Volcanology and Geothermal Research, 357, 56–67. https://doi.org/10.1016/j.jvolgeores.2018.04.004

Tierz, P., Clarke, B., Calder, E. S., Dessalegn, F., Lewi, E., Yirgu, G., et al. (2020). Event Trees and Epistemic Uncertainty in Long-Term Volcanic Hazard Assessment of Rift Volcanoes: The Example of Aluto (Central Ethiopia). Geochemistry, Geophysics, Geosystems, 21(10). https://doi.org/10.1029/2020GC009219

Viveiros, F., Cardellini, C., Ferreira, T., Caliro, S., Chiodini, G., & Silva, C. (2010). Soil CO2 emissions at Furnas volcano, São Miguel Island, Azores archipelago: Volcano monitoring perspectives, geomorphologic studies, and land use planning application. Journal of Geophysical Research: Solid Earth, 115(12), 1–17. https://doi.org/10.1029/2010JB007555

Weiss, R. F. (1968). Piggyback sampler for dissolved gas studies on sealed water samples. In Deep Sea Research and Oceanographic Abstracts (Vol. 15, pp. 695–699). Elsevier.

Werner, C., Brantley, S. L., & Boomer, K. (2000). CO2 emissions related to the Yellowstone volcanic system 2. Statistical sampling, total degassing, and transport mechanisms. Journal of Geophysical Research: Solid Earth. https://doi.org/10.1029/1999jb900331

Werner, C., Hurwitz, S., Evans, W. C., Lowenstern, J. B., Bergfeld, D., Heasler, H., et al. (2008). Volatile emissions and gas geochemistry of Hot Spring Basin, Yellowstone National Park, USA. Journal of Volcanology and Geothermal Research, 178(4), 751–762. https://doi.org/10.1016/j.jvolgeores.2008.09.016

Werner, Cynthia, & Cardellini, C. (2006). Comparison of carbon dioxide emissions with fluid upflow, chemistry, and geologic structures at the Rotorua geothermal system, New Zealand. Geothermics, 35(3), 221–238. https://doi.org/10.1016/j.geothermics.2006.02.006

Wilks, M., Kendall, J. M., Nowacki, A., Biggs, J., Wookey, J., Birhanu, Y., et al. (2017). Seismicity associated with magmatism, faulting and hydrothermal circulation at Aluto Volcano, Main Ethiopian Rift. Journal of Volcanology and Geothermal Research, 340, 52–67. https://doi.org/10.1016/j.jvolgeores.2017.04.003

Wolfenden, E., Ebinger, C., Yirgu, G., Deino, A., & Ayalew, D. (2004). Evolution of the northern Main Ethiopian rift: Birth of a triple junction. Earth and Planetary Science Letters, 224(1–2), 213–228. https://doi.org/10.1016/j.epsl.2004.04.022